Computers in Biology and Medicine 191 (2025) 110134

Contents lists available at ScienceDirect

Computers in Biology and Medicine

journal homepage: www.elsevier.com/locate/compbiomed

# Modelling of thrombus formation, growth and embolisation in the left atrial appendage under atrial fibrillation

Anna Maria Lo Presti [a,b,1], Alessandra Monteleone [b,1], Giulio Musotto [b], Alessandro Tamburini [a], Enrico Napoli [a], Gaetano Burriesci [a,b,c,*]

[a] University of Palermo, Department of Engineering, Palermo, Italy
[b] Ri.MED Foundation, Palermo, Italy
[c] UCL Mechanical Engineering, University College London, London, UK

ARTICLE INFO

*Keywords:*
Left atrial appendage (LAA)
Atrial fibrillation (AF)
Thromboembolic risk
Thrombus formation
Smoothed particle hydrodynamics (SPH)
Fluid-structure interaction (FSI)

ABSTRACT

Left atrial appendage (LAA) thrombosis is a frequent and serious complication associated with atrial fibrillation (AF), which significantly increases the risk of ischemic events. The presence of a thrombus within the LAA can disrupt normal blood flow and eventually embolise, leading to impaired circulation and severe complications.

An innovative fluid-structure interaction model, based on the smoothed particle hydrodynamics method, is used to simulate the formation and behaviour of thrombi in a patient-specific LAA morphology under AF condition. The clotting process is modelled by tracking the concentrations of key components involved in the coagulation cascade. The approach transforms fluid particles into a solid phase by applying internal spring forces when specific biochemical and haemodynamic conditions occur.

The findings shed light on the haemodynamic and biochemical mechanisms driving thrombus formation and migration within the LAA, highlighting regions of clot growth and subsequent embolisation. Thrombus formation begins at the LAA tip, gradually expanding through lobes and trabeculae, and ultimately progressing internally to high-recirculation regions, increasing the risk of embolisation and of potential clinical complications.

By accurately predicting thrombus formation, growth and fragmentation, this study offers valuable insight into the mechanisms associated with the thromboembolic risk in AF. These are crucial for developing targeted therapeutic strategies to minimise the risk of thromboembolic events in patient with AF.

## 1. Introduction

Atrial fibrillation (AF) is a common cardiac arrhythmia [1] characterised by rapid, irregular, and disorganised electrical impulses originating in the atria [2]. These abnormal impulses disrupt the natural pacemaker of the heart (the sinoatrial node) leading to inefficient atrial contractions and impaired blood flow to the ventricles [2]. AF is estimated to affect around 40 million people worldwide [1]. Since age is one of the most significant risk factors and global life expectancy continues to increase, AF prevalence is expected to increase of 50 % by 2050 [1]. The pathology is associated with stroke, heart failure, myocardial infarction, dementia, and chronic kidney disease [3], with stroke and thromboembolism identified as the most prevalent complications [4,5]. These are related with the increased risk of thrombus formation caused by the chaotic AF heart rhythm, which leads to blood stasis in the upper chambers of the heart [5]. In particular, approximately 90 % of clots responsible for thromboembolic events in AF originate in the left atrial appendage (LAA) [5,6]. This is a pouch-like structure protruding from the left atrium, characterised by a large morphological variability [7] and commonly classified based on its shape into four classes: chicken wing, cactus, windsock, and cauliflower [8].

Blood coagulation is regulated by a complex, multi-phase biochemical process known as the coagulation cascade [9], which involves the synergic action of several cellular and molecular components to create a stable clot. AF disrupts this finely balanced coagulation system, inducing a pro-thrombotic state [10] through mechanisms described in Virchow's triad [11] (this highlights hypercoagulability, endothelial injury, and stasis as contributing factors).

To prevent thrombus formation in AF, several treatment options are available: oral anticoagulants [12,13], LAA surgical exclusion [14], percutaneous LAA occlusion [15], and transcatheter ablation [16]. Since

* Corresponding author. University of Palermo, Department of Engineering, Viale delle Scienze, Ed. 8, 90128, Palermo, Italy.
*E-mail address:* gaetano.burriesci@unipa.it (G. Burriesci).
[1] Contributed equally.

https://doi.org/10.1016/j.compbiomed.2025.110134
Received 9 December 2024; Received in revised form 25 March 2025; Accepted 2 April 2025
Available online 7 April 2025

**List of abbreviations**

| | |
|---|---|
| ap | activated platelets |
| bp | bound platelets |
| $C_{\{pt,th,fg,fi\}}$ | concentration (nM) |
| $C_{\{rp,ap,bp\}}$ | concentration (PLT ml$^{-1}$) |
| $C_w$ | concentration at the wall (nM or PLT ml$^{-1}$) |
| $C^*_{th}$ | threshold concentration for thrombin (M) |
| $C^*_{bp}$ | threshold concentration for bound platelets (PLT ml$^{-1}$) |
| $C_{fi,50}$ | half-saturation constant for fibrin (nM) |
| $C_{th,50}$ | half-saturation constant for thrombin (nM) |
| $d_{0,ij}$ | spring resting length (m) |
| $d_{ij}$ | instantaneous distance between particles $i$ and $j$ |
| $f$ | force (N) |
| fg | fibrinogen |
| fi | fibrin |
| $G_1$ | groove |
| h | smoothing length (m) |
| i | particle of reference |
| $j$ | neighbouring particles |
| k | constant of the *kernel function* (−) |
| $k^{rp}_{th}$, $k^{ap}_{th}$ | constant kinetics (U PLT$^{-1}$ s$^{-1}$ $\mu$ M$^{-1}$) |
| $k^{th}_{fi}$, $k_{bp}$ | constant kinetics (s$^{-1}$) |
| $K^{th}_{m,fi}$ | constant kinetics (nM) |
| $K_{\{1,2,3\}}$ | knees |
| $k_e$ | spring constant (−) |
| $L_{\{1,2a,2b,3a,3b,3c\}}$ | lobes |
| m | mass of the particle (kg) |
| N | number of particles |
| $P_{\{1,2,3,4,5\}}$ | partitions of the LAA |
| pt | prothrombin |
| rp | resting platelets |
| r | time instant |
| $S_{\{pt,th,fg,fi,rp,ap,bp\}}$ | source term of the species |
| t | time (s) |
| $T_{\{1,2,3\}}$ | trabeculae |
| $t_{act}$ | time required for platelet activation (s) |
| th | thrombin |
| **u** | velocity (m s$^{-1}$) |
| **x** | position (m) |
| W | Kernel function |

*Greek symbols*

| | |
|---|---|
| $\alpha_{\{pt,thfg,fi,rp,ap,bp\}}$ | diffusion coefficient (cm$^2$ s$^{-1}$) |
| $\varphi$ | generic function |
| $\Phi^{th}_{ap}$, $\Phi^{fi}_{bp}$ | Hill functions |
| ρ | density (kg m$^{-3}$) |
| Ω | Support domain |

*Mathematical symbols*

| | |
|---|---|
| Δ | Delta operator |
| $\sum$ | Summation operator |
| $\nabla$ | Nabla operator |
| $\frac{\partial}{\partial t}$ | Partial derivative with respect to time |
| $\frac{D}{Dt}$ | material derivative with respect to time |

*Acronyms*

| | |
|---|---|
| AF | Atrial fibrillation |
| BSF | Blood stasis factor |
| CFD | Computational fluid dynamics |
| ECAP | Endothelial cell activation potential |
| FSI | Fluid-structure interaction |
| LA | Left atrium |
| LAA | Left atrial appendage |
| LIC | Line integral convolution |
| OSI | Oscillatory shear index |
| RRT | Relative residence time |
| SPH | Smoothed particle hydrodynamics |
| SSR | Shear strain rate |
| TAWSS | Time-averaged wall shear stress |
| WSS | Wall shear stress |

each option is associated with specific risks, it is crucial to assess patient's specific factors to select the most appropriate individualised treatment strategy. Currently, the $CHA_2DS_2$-VASc score [17] is used in clinical practice to assess thromboembolic risk in patients. This considers factors such as congestive heart failure, hypertension, age, diabetes mellitus, stroke, vascular disease, and gender. However, this guideline does not account for haemodynamic factors, which also play a crucial role in thrombus formation.

In recent years, numerous computational studies were conducted to explore the correlation between haemodynamic parameters and thrombus formation. Zhang and Gay [18] were the first to numerically analyse the haemodynamic parameters and characterise LAA function, showing that it becomes a site for blood stasis during AF, significantly increasing the risk of thrombosis. Moreover, the highly variable shape of the LAA has suggested that its morphology may be a risk factor for thrombus development. Several computational fluid dynamics (CFD) studies (Koizumi et al. [19]; Otani et al. [20]; Olivares et al. [21]; Bosi et al. [22]; Masci et al. [23]) explored the relationship between thrombogenicity and the four types of the LAA morphologies [8]. These haemodynamic studies use a rigid wall assumption, which may miscalculate the risk of thromboembolism by neglecting the dynamic nature of the wall and the reciprocal interaction with the blood. In this framework, Vella et al. [24], Kjeldsberg et al. [25] and Zingaro et al. [26], incorporating patient-specific LAA wall motion into their simulations, demonstrated that LAA compliance significantly affects flow patterns and must be considered in CFD simulations. Masci et al. [27], using a patient-specific CFD model that integrates atrial wall motion, demonstrated that AF-induced alterations in wall motion lead to reduced washout in the LAA, which may contribute to thrombosis formation. Similarly, Garcia Villalba et al. [28], comparing fixed and moving-wall simulations, showed that neglecting wall motion significantly impacts on the prediction of blood residence time and thrombotic risk.

Musotto et al. [29] introduced the use of fluid-structure interaction (FSI) studies on patient-specific LAA models, investigating the effects of AF-induced changes in contractility and anatomical shape. They found that the active contractility of the LAA is essential for maintaining healthy blood flow, and that its dysfunction, due to AF, contributes to the thrombosis risk. Their follow-up study [30], analysing 12 patient-specific models, revealed that significant differences exist even within the same morphological class, suggesting that current classification based solely on overall morphology is inadequate. Conversely, local features such as lobes and trabeculae can have a significant impact on the flow and thrombus formation.

Haemodynamic parameters based on wall shear stress (WSS), such as time-averaged wall shear stress (TAWSS), oscillatory shear index (OSI), endothelial cell activation potential (ECAP) and relative residence time (RRT) have been widely used to assess thrombosis risk [31–37]. For instance, Yang et al. [38] found that the RRT in the LAA was generally higher in AF than in sinus rhythm, confirming a higher thrombosis risk

prediction in AF patients. Chen et al. [39] demonstrated that variations in TAWSS predominantly occur at the LAA entrance, whereas OSI and other indicators like ECAP and RRT are more pronounced at the tip of the LAA, influenced by geometric features such as curvature. These studies suggest that ECAP and RRT are reliable parameters for assessing thrombotic risk, but they did not provide precise thresholds to define high or low risk. In this context, Musotto et al. [30] introduced a new parameter, named blood stasis factor (BSF), to specifically quantify thrombosis risk in the LAA. BSF measures the LAA surface area that constantly experiences shear strain rates below 5 $s^{-1}$, suggested as a critical threshold associated with prolonged blood stagnation during AF. Paliwal et al. [40] compared the geometrical and haemodynamic parameters of the left atrium and LAA in 28 paroxysmal AF patients who had a stroke versus 27 who had not, and found that the stroke group exhibited significantly lower blood velocity, lower WSS, and higher ECAP in the LAA. This suggests that the slow, oscillatory flow in the LAA experienced by stroke patients promotes endothelial cell activation and initiates the coagulation cascade, eventually leading to thrombus formation [41].

As hypercoagulability is also a critical contributor to thrombosis [11], Zhang et al. [42] examined the effects of blood rheology on LAA haemodynamics and found that the average blood viscosity in the LA and LAA was significantly higher than the constant viscosity typically assumed in simulations. This aligns with findings from Gonzalo et al. [43], who showed that assuming Newtonian behaviour for blood underestimates the thrombosis risk. On the other hand, Musotto et al. [30] verified that applying the Newtonian assumption to model blood flow in the LAA does not produce substantial differences in the results compared to more complex models, such as Casson's, and may lead to more conservative prediction of the thrombosis risk.

Patient-specific computational blood-flow analyses offer the potential to identify these haemodynamic conditions and aid in clinical stroke risk assessment. However, translating CFD simulations into clinical practice remains challenging due to their computational complexity and high cost. To address this, Gao et al. [44] and Liu et al. [45] proposed neural networks to predict multiple haemodynamic indices from point cloud data of patient-specific LAA geometries. This approach may offer a computationally efficient way to assess thrombotic risk in clinical settings, predicting key flow metrics such as velocity and pressure fields.

Despite these advances, most studies to date have focused on assessing the risk of thrombus formation in the LAA, rather than simulating the thrombosis process itself. This study addresses this gap by employing a mono-physics FSI model based on the smoothed particle hydrodynamics (SPH) method to simulate thrombus formation in patient-specific LAA morphologies under AF conditions. SPH was specifically chosen for its ability to model dynamic multiphase flows, which makes it particularly suitable for simulating thrombus dynamics and emboli movement. These processes are challenging to capture effectively with more traditional Eulerian CFD methods.

Originally developed for astrophysical problems [46], SPH is a meshless Lagrangian method which has gained popularity in bioengineering applications [47] thanks to its ability to handle complex geometries, large deformations, and evolving interfaces. This method has already been applied to the study of thrombosis [48–51]. Ye et al. [50] simulated two crucial steps in the initial stage of thrombus formation, *i.e.* platelet adhesion and aggregation, providing the first direct simulation of three modes of platelet adhesion. Al-Saad et al. [49] studied blood flow behaviour and explored conditions that induce thrombus formation in blood vessels. To simulate thrombogenesis, they modelled blood with two sets of particles representing plasma and platelets, and used an inter-particle force model to simulate platelet adhesion and aggregation. Wang et al. [48] introduced a simplified method based on a velocity decay factor to simulate changes in fibrin concentration using a convection-diffusion equation, without accounting for fibrin diffusivity or reaction sources. Monteleone et al. [51] developed a thrombus formation model considering four biochemical species and three types of platelets to replicate the main steps of the coagulation cascade. They implemented a novel mono-physics FSI approach introducing elastic forces between solid particles, activated by the recruitment of fluid particles under specific hydrodynamic and biochemical conditions. This model was applied to simulate thrombus formation in a backward facing step, and validated by comparing numerical results with experimental data available in the literature [52].

In the present study, the approach developed by Monteleone et al. [51] is employed to simulate thrombus formation within the LAA. Unlike previous studies that primarily estimate thrombosis risk based on haemodynamic parameters [30–40,44,53–56] or focus on static mural thrombus [57], this work goes further by simulating, for the first time, the entire process of thrombus formation, growth and fragmentation, modelling its dynamic interaction with the blood flow within the LAA. By providing new insights into the mechanisms and evolution of thrombus dynamics, the study aims to advance the understanding of these processes, essential for improving risk stratification and optimising patient management.

## 2. Materials and methods

### 2.1. SPH scheme

As mentioned in the introduction, the present study employs the SPH method, integrated within the software PANORMUS (PArallel Numerical Open-souRce Model for Unsteady flow Simulations), to simulate thrombus formation. In SPH, the computational domain is represented by a set of particles. The variables at each particle are determined through interpolation via a *kernel function*, $W$, whose influence is defined by a *smoothing length*, $h$. Specifically, the value of a generic function $\varphi$ at particle $i$, located at position $\mathbf{x}_i$, is obtained by interpolating the values of the neighbouring particles $j$ (1), whose distance from particle $i$ is less than $k{\cdot}h$, where $k$ is a constant which depends on the specific *kernel function* employed (in this study, the Wendland function [58] was used, where $k$ is equal to 2):

$$\varphi_i = \sum_{j=1}^{N_i} \frac{m_j}{\rho_j} \varphi_j W_{ij} \tag{1}$$

In Eq. (1), $N_i$. is the total number of particles in the support domain of $i$ ($\Omega_i$), $m_j$ and $\rho_j$ represent the mass and density of $j$, respectively, and $W_{ij} = W(\mathbf{x}_i - \mathbf{x}_j, h)$. In this work, particles are initially distributed at a spacing $\Delta x = k{\cdot}h/2$, as recommended in the literature [59–62].

This work adopts an incompressible SPH (ISPH) approach to solve the momentum and continuity equations. In particular, the pressure field is determined implicitly by solving a system of pressure Poisson equations (PPEs) using the BiConjugate Gradient Stabilized method (BiCGSTAB) proposed by Van der Vorst [63], following the fractional-step technique of Chorin [64], in which the velocity field is first predicted using an intermediate step that neglects pressure. Then, in the second step, a pressure correction is applied to enforce incompressibility, adjusting the predicted velocities to ensure mass conservation. Further details on the employed fractional-step procedure and methodology can be found in Monteleone et al. [62].

Boundary conditions, which are notoriously difficult to impose in SPH due to the truncation of the particle support domain near boundaries, are handled by using the mirror particle technique [59]. Particles having distance from the boundaries shorter than $k{\cdot}h$ are mirrored along the direction normal to the boundaries. The mirror particle has the same physical properties of the parent particle, while velocity or pressure are imposed to ensure the satisfaction of the required boundary conditions. This technique allows for accurate modelling of boundary conditions, even in complex geometries, by preventing voids or non-physical behaviour at the domain boundaries. For a comprehensive description of the mirror particle procedure, see Napoli et al. [59] and Monteleone

et al. [62].

To address another challenge in SPH, namely *tensile instability* [65], which can lead to particle clustering, this study uses a correction method where particles are slightly shifted across streamlines, as suggested by Xu et al. [66], to ensure a more uniform particle distribution. This correction is crucial for maintaining the overall stability of the simulation, preventing the formation of localised particle clusters or voids that could affect fluid dynamics. Ensuring an even particle spacing helps to preserve the accuracy of the velocity and pressure fields, particularly in regions where high gradients are present. A detailed explanation of this correction method, including its effectiveness in preventing instability, can be found in Xu et al. [66].

### 2.2. Thrombus modelling

Thrombus formation is predominantly governed by the coagulation cascade, which can be initiated through either the extrinsic or intrinsic pathways [67]. The extrinsic pathway is triggered by endothelial injury, which exposes tissue factor (TF), a crucial protein that initiates the coagulation process. Moreover, the injury of endothelium releases von Willebrand factor (vWF) [68] into the plasma, leading to trace thrombin formation, a key enzyme in the clotting process, from prothrombin, an inactive precursor of thrombin. The intrinsic pathway is auto-initiated and begins with the activation of plasma factors XII, XI, IX, and VIII. Both pathways ultimately converge by activating factor X, which marks the beginning of the common pathway [67]. Once factor X is activated, the process moves to the amplification and propagation phases, where platelets become activated, leading to large-scale thrombin generation. This thrombin cleaves fibrinogen, a soluble plasma protein, into insoluble fibrin monomers [10]. In the final stabilisation phase, polymerised fibrin traps platelets and red blood cells, forming a haemostatic plug that, under normal conditions, facilitates healing [69].

The thrombus formation model employed in this work is summarised in the following (refer to Ref. [51] for more details). As mentioned above, the model considers the final stages of the coagulation cascade, common to the intrinsic and extrinsic pathways. Specifically, four key biochemical species (prothrombin – pt, thrombin – th, fibrinogen – fg, and fibrin – fi) and three types of platelets (resting platelets – rp, activated platelets – ap, and bound platelets – bp) are modelled. Thrombin is considered the only agonist species, promoting both the conversion of fibrinogen to fibrin and the activation of resting platelets. Platelet activation is modelled through a function of local agonist concentrations, defined in the kinetic constant $k_{ap}$. This constant, along with other parameters such as diffusion coefficients and concentration values, is reported in Table 1.

The transport of the analysed species is evaluated by solving the advection-diffusion equation, reported below in Lagrangian formulation [75–82]:

$$\frac{DC_s}{Dt} = \alpha_s \nabla^2 C_s + S_s \tag{2}$$

with the moving coordinate system

$$\frac{d\mathbf{x}}{dt} = \mathbf{u} \tag{3}$$

where $C_s$ represents the time-dependent concentration of a generic species (with s = pt, th, fg, fi, rp, ap, bp), $\alpha_s$ and $S_s$ are the diffusivity and the source term of the specie $s$, respectively, $\mathbf{x}$ indicate the position vector, while $\mathbf{u}$ the velocity vector. The material derivative $\frac{DC_s}{Dt} = \frac{\partial C_s}{\partial t} + \mathbf{u}\cdot\nabla C_s$, which includes the convective term in the Lagrangian formulation [83], represents time rate change of species concentration along the pathline of a particle.

The conversion from resting to activated platelets occurs when

**Table 1**
Key Reactions and source terms in coagulation pathway. For more details refer to Ref. [51].

| Chemical reaction | Source terms | Constants | Diffusion coefficients | Biochemical concentrations |
|---|---|---|---|---|
| **1. Thrombin generation** $pt + rp \rightarrow^{k_{th}^{rp}} th$ $pt + ap \rightarrow^{k_{th}^{ap}} th$ | $S_{th} = k_{th}^{rp} C_{rp} C_{pt} + k_{th}^{ap} C_{ap} C_{pt}$ $S_{pt} = -S_{th}$ | $k_{th}^{rp} = 6.50 \bullet 10^{-10}$ U PLT$^{-1}$ s$^{-1}$ $\mu$ M$^{-1}$ [70] $k_{th}^{ap} = 3.69 \bullet 10^{-10}$ U PLT$^{-1}$ s$^{-1}$ $\mu$ M$^{-1}$ [70] | $\alpha_{th} = 6.47 \cdot 10^{-7}$ cm$^2$ s$^{-1}$ [71] | $C_{pt} = 1400$ nM [72] |
| **2. Conversion of fibrinogen to fibrin** $fg + th \rightarrow^{k_{fi}^{th}} fi$ | $S_{fi} = \frac{k_{fi}^{th} C_{th} C_{fg}}{K_{m,fi}^{th} + C_{fg}}$ $S_{fg} = -S_{fi}$ | $k_{fi}^{th} = 59$ s$^{-1}$ [71] $K_{m,fi}^{th} = 3160$ nM [71] | $\alpha_{fi} = 2.47 \cdot 10^{-7}$ cm$^2$ s$^{-1}$ [71] | $C_{fg} = 7000$ nM [72] |
| **3. Conversion of resting platelets in activated platelets** $rp \rightarrow^{k_{ap}} ap$ $th \rightarrow^{k_{ap}^{th}} ap$ | $S_{ap} = k_{ap} C_{rp} + k_{ap}^{th} \phi_{ap}^{th***} C_{rp}$ $S_{rp} = -k_{ap} C_{rp} - k_{ap}^{th} \phi_{ap}^{th} C_{rp}$ | $k_{ap} = \begin{cases} 0, \Omega < 1 \\ \frac{\Omega^*}{t_{act}^{**}}, \Omega \geq 1 \end{cases}$ | $\alpha_{ap} = 2.5 \cdot 10^{-7}$ cm$^2$ s$^{-1}$ [73] | $C_{rp} = 2 \cdot 10^8$ PLT ml$^{-1}$ [72] $C_{th}^* = 9.11 \cdot 10^{-10}$ M [70] |
| **4. Formation of bound platelets** $fi + ap \rightarrow^{k_{bp}} bp$ | $S_{bp} = k_{bp} \phi_{bp}^{fi****} C_{ap}$ $S_{ap} = -k_{bp} \phi_{bp}^{fi} C_{ap}$ | $k_{bp} = 1 \bullet 10^4$ s$^{-1}$ [73] | $\alpha_{bp} = 0$ [72] | $C_{ap} = 1 \cdot 10^7$ PLT ml$^{-1}$ [72] $C_{fi,50} = 600$ nM [72] |

pt: Prothrombin, th: Thrombin, fg: Fibrinogen, fi: Fibrin, rp: Resting Platelets, ap: Activated Platelets, bp: Bound Platelets, k: Rate constant, S: Source terms.
Notes.

* $\Omega = \sum_{s=1}^{N_s} w_s \frac{C_s}{C_s^*}$, is a function of local agonist concentrations that evaluates the impact of each single specie on the rate of platelet activation [70]. Specifically, $w_s$ is the weight assigned to the agonist s, $C_s$ is the concentration of the agonist s and $C_s^*$ is the threshold value for the concentration of s. In this model, $\Omega = w_{th} \frac{C_{th}}{C_{th}^*}$, $w_{th} = 1$ and $C_{th}^*$ is the threshold concentration of thrombin.

** $t_{act} = 1$ s, denotes the time required for platelet activation [70].

*** $\phi_{ap}^{th} = \frac{C_{th}^4}{C_{th}^4 + C_{th,50}^4}$, is a fourth-order Hill function used to model processes involving cooperative binding [72], $C_{th,50} = C_{th}^*$ is the half-saturation constant, representing the thrombin concentration at which half-maximal binding occurs [74].

**** $\phi_{bp}^{fi} = \frac{C_{fi}^2}{C_{fi}^2 + C_{fi,50}^2}$, is a second-order Hill function used to model processes involving cooperative binding [74], $C_{fi,50}$ is the half-saturation constant, representing the fibrin concentration at which half-maximal binding occurs [74].

thrombin concentration exceeds the threshold value $C^*_{th}$, which is set to $9.11 \times 10^{-10}$ M, as recommended in the literature [70,84].

Activated platelets connected to the fibrin network generate bound platelets. As will be discussed in section 2.3, a threshold limit for bound platelet (indicated as $C^*_{bp}$) is used to determine if fluid particles shall be switched to solid phase. This threshold concentration, that merely regulates the simulation timescale without altering the thrombus formation mechanism, is equal to $6 \times 10^{15}$ PLT m$^{-3}$, as in Ref. [51].

Thrombus formation is triggered when two of the three components of Virchow's triad [11] —endothelial injury, hypercoagulability, or stasis— are simultaneously present. In this model, endothelial injury is considered the primary factor initiating thrombus formation, and thrombin specie to have the dominant role in the coagulation process (driving platelet activation, fibrin mesh formation, and platelet binding). Therefore, in order to simulate the injured area and initiate thrombus formation, the triggering is imposed for the first two cycles (with period T = 0.86 s corresponding to a standard beat rate of 70 bpm) as flux boundary conditions for thrombin concentration at the LAA wall. Specifically, the concentration of thrombin at the LAA wall is artificially elevated above the physiological values ($C_{w,th}$). Following the mirror particle technique, to impose $C_{w,th}$, the concentration of the mirror particle ($C_{m,th}$) is set equal to $2C_{w,th} - C_{g,th}$, where $C_{g,th}$ is the concentration of the generating particle (for more details see Monteleone et al. [51]). From the third cycle (when the injured wall is removed), homogeneous Neumann conditions are imposed at the LAA opening and at the LAA wall for the concentration of all the species $\frac{\partial C_s}{\partial n} = 0$; where n is the direction normal to the boundary (pointing towards the interior of the domain). This is achieved by imposing the concentrations of the mirror particle equal to that of the generating particle $\left(C_{m,s} = C_{g,s}\right)$ [51].

In the model, shear strain rate (SSR), which measures the rate of tangential deformation between adjacent fluid layers, was considered to have a crucial role in the thrombus formation process. In particular, low levels of SSR are correlated with blood stasis [56,85,72]. For this reason this hydrodynamic parameter is commonly used to assess the risk of thrombosis in computational studies [29,30,56,72].

In order to accelerate the thrombus formation process, which typically evolves over minutes to hours [86], the diffusion of species is amplified using a numerical coefficient related to the SSR. Specifically, as described in Ref. [51], this coefficient is a function of the SSR ensuring that the amplification mechanism is selectively activated in regions of blood stasis, where thrombus formation is more likely to occur. As a consequence of this numerical enhancement, the simulated cycle does not correspond temporally to the cardiac cycle; therefore, hereinafter it will be indicated as *numerical cycle*.

Due to the accelerated conversion of thrombin, a continuous supply of the inactive biochemicals (pt and fg) and resting platelets was imposed in the simulation.

The concentrations of the modelled species were initialised based on typical values found in healthy human blood, as reported in Table 1, except for thrombin, fibrin, and bound platelets, which were set to zero. To replicate primary haemostasis, an initial amount of activated platelets was introduced, equal to 5 % of the resting platelet background concentration, as recommended by Sarrami-Foroushani et al. [72].

### 2.3. Mono-physics FSI

This work employs a mono-physics FSI model [87], where fluid-solid coupling is incorporated within the modelling framework, in which both fluid and solid particles are solved concurrently within a unified ISPH numerical scheme [51].

Initially, all particles behave as fluid particles (Fig. 1a), transitioning into solid particles when bound platelet concentration $C_{i,bp}$ exceeds a threshold $C^*_{bp}$. Spring links are thus introduced between neighbouring solid particles located within a distance $k{\cdot}h$ from particle $i$. In Fig. 1b,

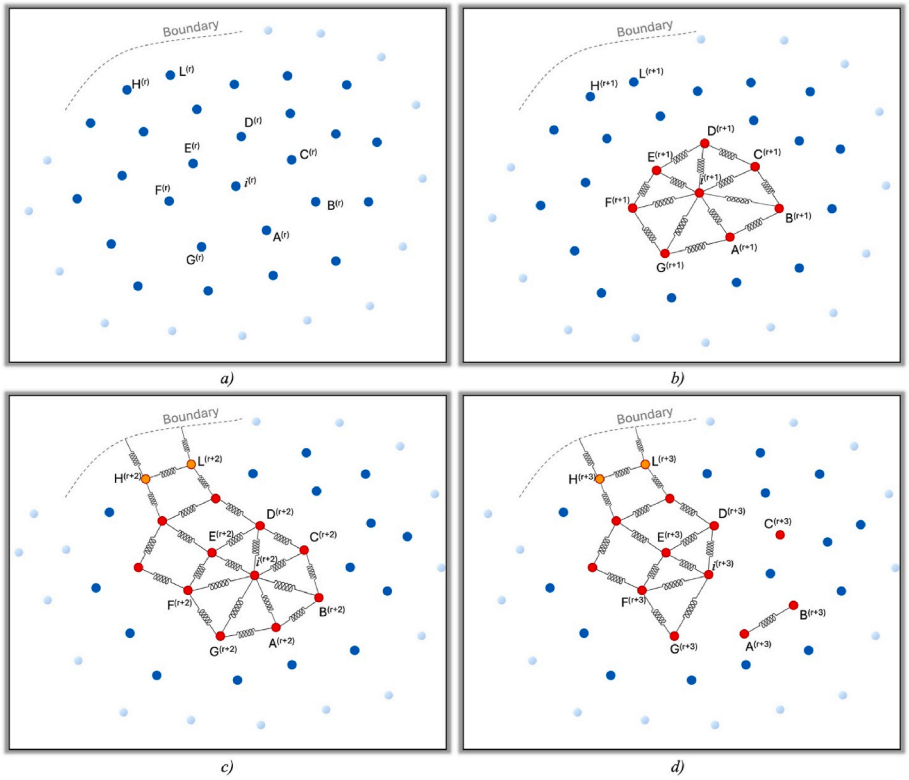


**Fig. 1.** Sketch of the thrombus formation. Blue circles: fluid particles, red circles: solid particles; orange circles: solid particles bounded to the wall. a) time instant (r); b) time instant (r+1); c) time instant (r+2); d) time instant (r+3). (For interpretation of the references to colour in this figure legend, the reader is referred to the Web version of this article.)

particle $i$ at time instant $(r+1)$ is bounded to the neighbouring solid particles (from A to G). When particle $i$ is converted into a solid particle, its position $x_{i,ref}$ is recorded as the new reference position for the calculation of the spring force. The total internal force $\mathbf{f}_i$ acting on a solid particle $i$, which is introduced into the momentum equations as a body force (specifically added in the predictor step of the ISPH approach), is expressed as:

$$\mathbf{f}_i = \frac{k_e \Delta x}{m_i} \sum_{j=1}^{N} \left(d_{0,ij} - d_{ij}\right) \hat{\mathbf{x}}_{ij} \tag{4}$$

where $N$ is the number of neighbouring solid particles connected to $i$, $d_{0,ij}$ is the spring resting length, $d_{ij}$ is the instantaneous distance between particles $i$ and $j$, $\hat{\mathbf{x}}_{ij} = \left(\mathbf{x}_i - \mathbf{x}_j\right)/d_{ij}$ is the unit vector directed from $i$ to $j$, and $k_e$ is the spring constant, normalised over the initial distance ($\Delta x$). The calibration of this force law, which relates $k_e$ to the mechanical properties of the thrombus structure, specifically to its Young's modulus, was performed by simulating uniaxial tensile tests on a solid cube, as described in Monteleone et al. (2022) [88] and Monteleone et al. (2023) [51] (see these references for more detailed information about the methodology and mechanical properties employed). Differently from Monteleone et al. (2023) [51], where the rest length of the spring was set equal to $\Delta x\sqrt{2}$, representing the average inter-particle distance in the initial configuration, in this study the rest distance $d_{0,ij}$ is defined as the distance between the reference positions of particles $i$ and $j$ $\left(\mathbf{x}_{i,ref} - \mathbf{x}_{j,ref}\right)$. This choice was found to have no significant impact on the simulation results, while improving numerical stability.

Fig. 1c represents a schematic of the thrombus growth which occurs by adding spring links to the newly formed solid particles. Solid particles having a distance shorter than $k{\cdot}h$ from the wall are bounded to the wall by introducing spring links (particles H and L in Fig. 1c). Potential fragmentation of the thrombus is shown in Fig. 1d. Once formed, a spring can stretch up to a critical force limit, $\mathbf{f}_{max}$, beyond which the bond between two particles is released. The force limit influences the maximum elongation of the springs, and it is independent from the resting length. This allows for individual particles (see particle C in Fig. 1d) or clusters of particles (see particles A and B in Fig. 1d) to detach from the main thrombus and embolise.

### 2.4. Geometry and boundary conditions

In this work, geometry of LAA and boundary conditions were taken from the work of Musotto et al. [30], where twelve LAA models were analysed. In particular, a windsock-shape LAA (see Fig. 2), indicated as *windsock 1* in Musotto et al. [30], was considered for this simulation. This model was chosen because it includes all main morphological features of LAAs recognised to have a key role in the thrombus formation process (orifice, lobes, trabeculae, knees and grooves) [29]. To facilitate the identification of these local features, they are referred to using a letter and a number, as shown in Fig. 2 ('L' indicates main lobes, 'T' trabeculae, 'K' knees and 'G' grooves). Moreover, this LAA model has relatively small physical dimensions, resulting in the need of less particles, and reduced computational cost and simulation time.

To isolate the role of the appendage in the flow dynamics, only the LAA region was modelled. This simplification does not model the complex and highly unstable fluid dynamics established in the left atrium, which depends on several patient-specific anatomical factors (i.e. the LAA geometry, the number, shape and position of the pulmonary veins, mitral valve and LAA orifice) and assumptions (such as the specific pressure and flow conditions acting at the veins and valvular ostia). However, the effect of the atrial flow regime over the velocities and shear rates has been demonstrated to affect the results only in the immediate proximity of the LAA ostium, where the risk of thrombosis is negligible [22,24,29]. Therefore, the adopted simplification enhances the reproducibility and comparability of the analyses, while maintaining the necessary accuracy in the regions at risk of clot formation.

In Musotto et al. [30], pathological conditions were replicated through a one-way FSI analysis using the System Coupling module available on ANSYS Workbench [89], assuming as boundary conditions an impaired pressure curve (with period of the cardiac cycle T = 0.86 s) by AF patients without active contraction [90].

In this study, the atrial fibrillation condition was simulated in SPH imposing the LAA wall motion derived from the results of [30] as moving boundaries with adherence condition. Therefore, the velocity, $\mathbf{u}_m$, of the mirror particle was set equal to $\mathbf{u}_m = 2\,\mathbf{u}_w - \mathbf{u}_g$, where $\mathbf{u}_w$ is the velocity of the wall at the intersection point between the boundary and the line connecting the mirror with the generating particle, while $\mathbf{u}_g$ is the velocity of the generating particle [59].

Moreover, a zero-pressure reference condition was applied at the LAA inlet, modelled as an opening [62], allowing the flow to develop based on the pressure gradient established by the imposed wall movement [30].

The domain was discretised with a smoothing length of $5.5 \times 10^{-4}$ m, resulting into an average number of particles during the cycle equal to 167,779 (convergence analysis has confirmed that this resolution is

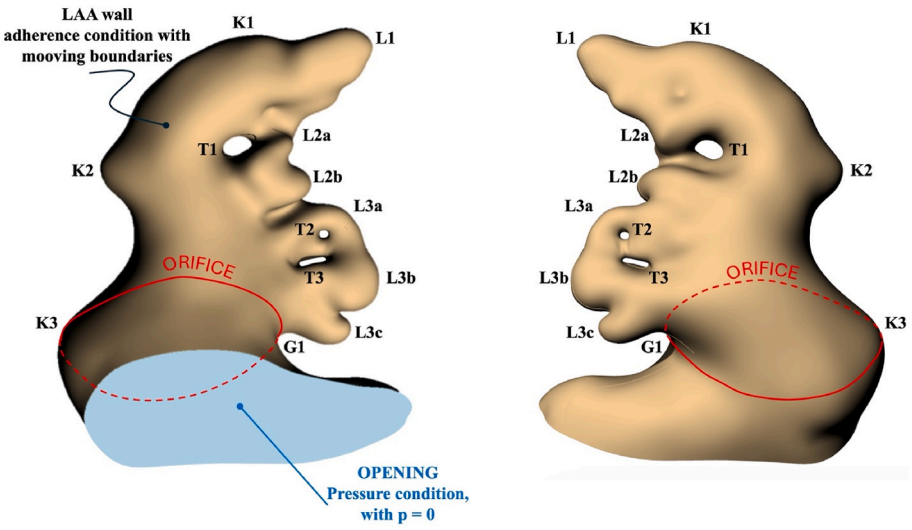


**Fig. 2.** LAA features and boundary conditions. Orifice: red line; lobes: L1, L2a, L2b, L2L3a, L3b and L3c; trabeculae: T1, T2 and T3; knees: K1, K2 and K3; groove: G1. (For interpretation of the references to colour in this figure legend, the reader is referred to the Web version of this article.)

adequate, resulting in average errors for the local velocity magnitude and concentrations, normalised by the maximum values, below 3 % for all quantities).

Blood was modelled as incompressible Newtonian, with dynamic viscosity of 0.0037 Pa s and a density of 1062 kg/m$^3$. This assumption reduces computational cost, without introducing significant differences compared to more accurate non-Newtonian formulations [30]. Moreover, it may underestimate the level of stagnation, resulting conservative in the prediction of thrombosis [43,91].

As discussed in section 2.2, injured wall condition was imposed only in the first two numerical cycles. Subsequently, this condition was removed and the thrombus started to form where the concentration exceeds the threshold value $C^*_{bp}$.

Overall, eighty (80) numerical cycles were simulated, stopping the analysis when no significant variations in the formed thrombus were observed for more than 5 cycles.

Simulation was carried out on an AMD EPYC 7402–2.8 GHz processor and the time to complete one cycle in serial mode was about 12 h. In order to save computational costs, the parallelisation scheme described by Monteleone et al. (2022) [92] can be implemented, by extending the approach to domains with moving boundaries.

## 3. Results and discussion

Due to the highly complex geometry of the patient-specific model (see Fig. 2), it is not possible to identify a single plane that shows all the LAA local features, including lobes and trabeculae. Therefore, for clarity of representation, results of the haemodynamic analysis are visualised over two cross sections laying on planes at different levels. As shown in Fig. 3, plane 1 illustrates the general coronal view, whilst plane 2 focuses on the trabeculae and lobes located on the left side of the domain, adjacent to the LAA orifice. Moreover, three key instants of the cardiac cycle are analysed in detail: the maximum velocity of contraction of the LAA wall ($t_1$) and the LAA minimum and maximum volume ($t_2$ and $t_3$, respectively).

### 3.1. Thrombus

Fig. 4 shows the thrombus formation percentage in the analysed domain over time, calculated as the ratio of solid particles to the average total number of particles during a cycle. Reported results will focus on nine cycles, useful to interpret the different stages of the phenomenon. These are selected subdividing the maximum value of the thrombus formation percentage into eight even steps (the corresponding number of cycles is highlighted in Fig. 4 from *a* to *i*). For simplicity, the nomenclature used for the panels in Figs. 5–8 corresponds to the indices adopted for the respective cycles in Fig. 4 (*e.g.* Fig. 7d represents *cycle d* as identified in Fig. 4).

For the first two cycles, when the injured wall is imposed (as discussed in section 2.2), no thrombus is formed, as the threshold concentration $C^*_{bp}$ is not reached in any region of the domain (from zero to point *a* in Fig. 4). After this initial stage, thrombus formation begins, and the curve exhibits a rapid nearly linear growth (*a*-*b*). To better describe this phase, three additional cycles between *a* and *b* (indicated as *a1*, *a2* and *a3*, corresponding to the 3$^{rd}$, 4$^{th}$ and 5$^{th}$ cycles, respectively) are analysed. Afterwards, the growth rate starts to reduce (*b*-*c*), with a noticeable deceleration in thrombus development from the 12$^{th}$ to the 20$^{th}$ cycle (*c*-*d*), until the formation reaches 16.66 % (*d*). From this point, the growth accelerates again. Subsequently, an inflection point is observed (*e*-*f*), marked by a change in slope, followed by another phase of linear growth over time (*f*-*g*). At the 62$^{nd}$ cycle (*h*), a sudden increase in thrombus formation is experienced, followed by another linear growth phase and a further step increase. This is associated with the formation of thrombus plugs that occlude the flow channel crossing the clotted region. This causes sudden stagnation of entire regions, activating several particles in a short time. This mechanism is responsible for the jumps observed in the *h*-*i* segment in Fig. 4. After the 74$^{th}$ cycle, thrombus formation stabilises, with variations below 0.02 % over 5

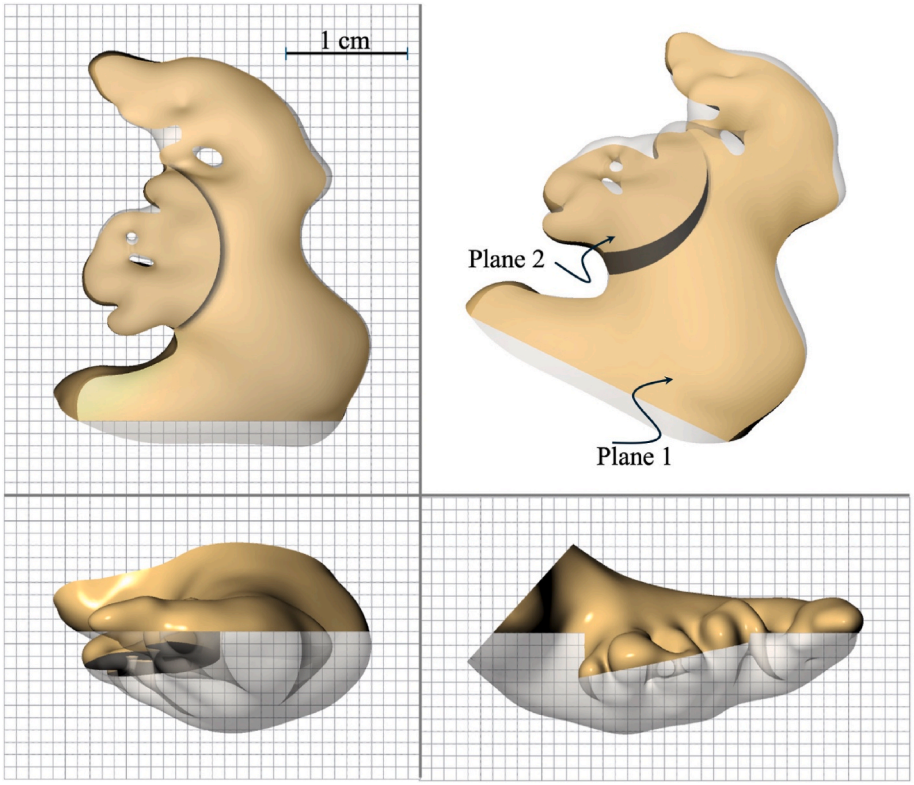


**Fig. 3.** Sketch of the plans used to report the results of the haemodynamic analysis.

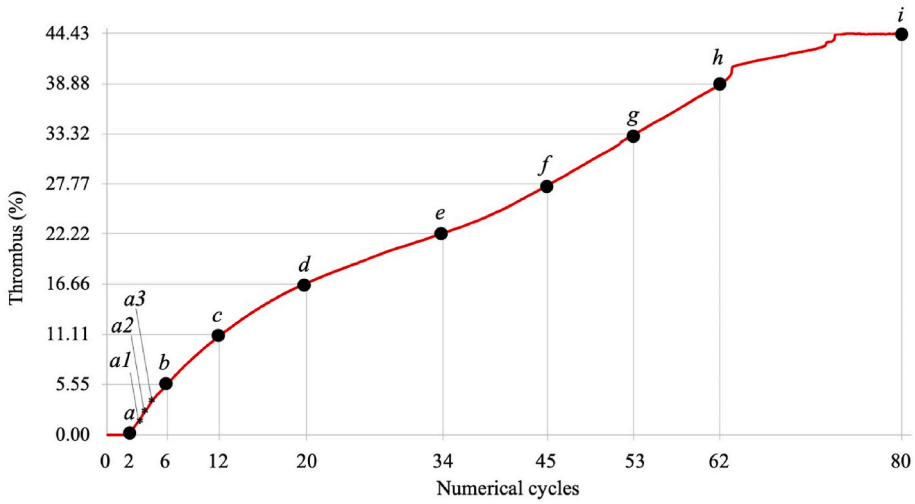


**Fig. 4.** Percentage of thrombus formed in the analysed domain over time, expressed in numerical cycles. a) 2nd cycle, a1) 3rd cycle, a2) 4th cycle, a3) 5th cycle, b) 6th cycle, c) 12th cycle, d) 20th cycle, e) 34th cycle, f) 45th cycle, g) 53rd cycle, h) 62nd cycle, i) 80th cycle.

cycles (*i*).

Fig. 5 illustrates the progression of thrombus formation in the entire three-dimensional model. Notably, the process begins at the tip of the LAA (lobe L1), confirming its high thrombogenicity due to blood stagnation. Thrombus formation then extends to the lobes L3b and L3c (*a1* in Fig. 5) before spreading further to lobes L2b and L3a, and to knees K1 and K2 (*a2* in Fig. 5). These findings are in agreement with clinical outcomes [93–95] and other computational works aimed at assessing the thromboembolic risk [37,96], where the LAA tip and lobes are recognised as high-risk regions. Initially, thrombus formation occurs at the wall, due to the thrombin boundary condition (imposed for the first two cycles, as described in section 2.2), which simulates the presence of wall injuries. Subsequently, the thrombus extends within the fluid domain. As thrombus formation advances, it interests lobe L2a and the area near knee K1 (see *a3* and *b* in Fig. 5), progressively spreading across the surface surrounding the LAA tip and reaching the surface of trabecula T1, as shown in Fig. 5c. In subsequent cycles, the thrombus continues to grow in the previously identified regions, both inside the LAA and along the wall, and starts forming also at the midspan of the appendage (Fig. 5d). The thrombus then occludes the area near trabecula T3 (Fig. 5e), penetrating inside and extending into adjacent areas. It eventually occupies the entire section of the LAA (Fig. 5f and g). In this phase, several particles embolise and leave the LAA, as shown by the white dots representing the embolised particles in Figs. 6–8. By *cycle h* in Fig. 5, the thrombus covers the appendage from tip to midspan, obstructing the flow channels inside the clotted region. In this stage, a layer of thrombus covering part of the LAA wall (at the side with lower SSR) expands to the orifice and starts propagating into the atrium. Finally, the thrombus stabilises (Fig. 5i), occupying nearly 45 % of the domain and 65 % of the LAA, defined as the volume up to the orifice (see Fig. 4). In this configuration, several particles embolise and leave the appendage (see white dots in Figs. 6i–8i).

### 3.2. Haemodynamic changes

As reported in section 2.2, SSR has a key role in the thrombus formation process. Figs. 6–8 show the continuous SSR maps on the two selected planes described in Fig. 3, at the maximum velocity of wall contraction ($t_1$) and at the minimum and maximum expansion of the LAA volume ($t_2$ and $t_3$, respectively). The SSR values, calculated by the SPH code at discrete particle positions, were processed and interpolated to generate continuous fields across each plane, ensuring a coherent representation of SSR. The velocity streamlines are also visualised in Figs. 6–8 using the line integral convolution (LIC), at the selected nine stages of the thrombus formation (from *a* to *i*) indicated in Fig. 4. Since the streamlines in the figures are influenced by the wall motion, SSR maps are useful to isolate the fluid dynamic contribution.

The thrombus front, indicated by dashed white lines on the maps, moves consistently with the wall position, appearing at different locations across the equivalent cycles (see for example in Fig. 6h and Fig. 8h). Internal flow channels crossing the clotted region are indicated with dotted lines, while embolised particles are represented as white dots.

In Fig. 6, it is evident how the presence of the thrombus significantly alters the haemodynamics in the LAA. The thrombus creates a wall effect resulting in an increase in the SSR, visible at the interface region separating liquid blood and thrombus (white dashed lines in Figs. 6–8). At the early stages (Fig. 6b), in correspondence of the thrombus located at lobe L1, SSR peaks of 10 $s^{-1}$ are observed, values that were absent before thrombus formation (Fig. 6a). As thrombus formation progresses, larger areas come into contact with the clot, leading to higher SSR levels over time (see Fig. 6b–f). This is particularly evident in the upper part of the domain, although the thrombus-blood interface also advances in the lower left section, near lobes L3b and L3c. Conversely, the internal region occupied by the clot, where particles behave like an elastic solid material, exhibits SSR values below 2 $s^{-1}$.

As the thrombus reaches the central region of the LAA (Fig. 6g), a progressive propagation of the thrombotic area with the surrounding regions becomes visible (Fig. 6h). In these latter stages, reaching the thrombus front a high-recirculation area, thrombi originating from lobe L3c begin to detach (see white points in Fig. 6f–i). This phenomenon is particularly noticeable in Fig. 7f–i, at the time $t_2$ corresponding to the minimum volume. The thrombus begins to detach at the maximum velocity of wall contraction ($t_1$), due to the higher SSR values. Later, during the phase of minimum expansion ($t_2$), these embolised solid particles are carried away, especially in the region around groove G1.

It should be highlighted that, although the most noticeable haemodynamic changes occur in the upper part of the LAA (particularly at the maximum contraction velocity), the area near lobe L3c appears to be the most dangerous. Here, constant exposure to high SSR increases the risk of thrombus detachment. When the thrombus detaches, it enters a region with higher recirculation and is easily channelled to the atrium, significantly increasing the risk of ischaemic events.

The most significant changes in lobes L3b and L3c are observed at the instant $t_3$ (Fig. 8). The presence of thrombus becomes evident, as increasingly larger areas are exposed to very low SSR values, accompanied by a change in the direction of the flow lines. As the thrombus reaches trabeculae T2 and T3 (Fig. 8c–e), SSR values drop below 1 $s^{-1}$,

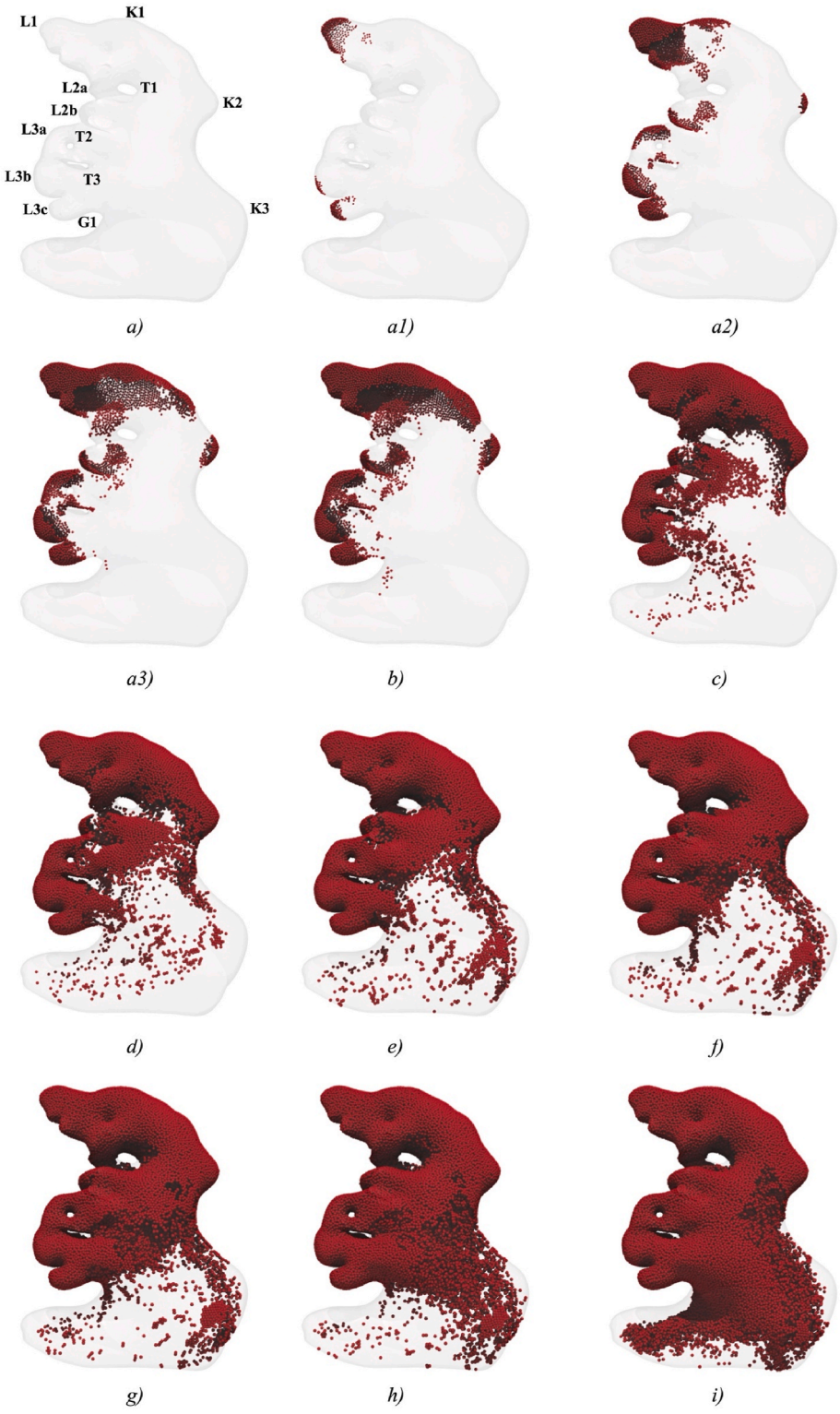


**Fig. 5.** *Thrombus formation in the numerical cycles a to i indicated in Fig. 4. The local features of the LAA are reported as in Fig. 2 ('L' indicates main lobes, 'T' trabeculae, 'K' knees and 'G' grooves).*

compared to approximately 3.0 $s^{-1}$ observed in the absence of clot (Fig. 8a). As the thrombus progresses towards lobes L3a, L3b and L3c, as well as to trabeculae T2 and T3 (Fig. 8f), it comes into contact with regions where SSR levels are higher (Fig. 8g and h). This causes the detachment of clot fragments (see white points in Fig. 8i), which then migrate within the fluid domain.

### 3.3. Species concentration

Fig. 9 shows the evolution of the of thrombin and activated platelet concentrations over the 80 numerical cycles, in five selected partitions (indicated as $P_1$, $P_2$, $P_3$, $P_4$ and $P_5$) of the LAA. For each partition, the concentrations of thrombin and activated platelets were calculated at the centroid, as mean value of the concentrations of the neighbouring

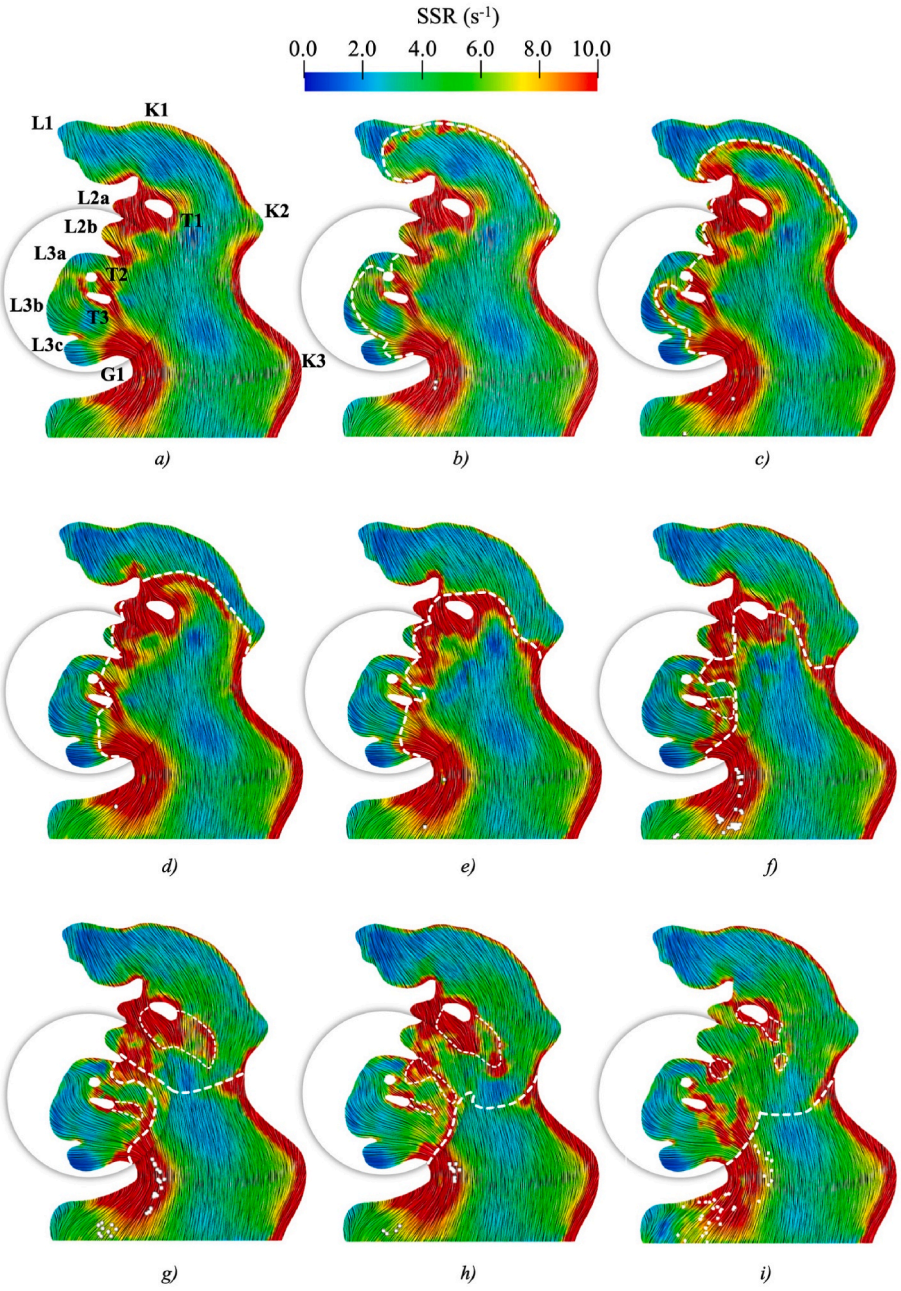


**Fig. 6.** *Continuous shear strain rate contour maps and velocity streamline at the time instant $t_1$ corresponding to the maximum velocity of contraction of the LAA wall. Bold white dashed line: thrombus front; thin white dashed line: internal flow channels wall. White dots: emboli. Numerical cycles a to i are indicated in* Fig. 4. *The local features of the LAA are reported as in* Fig. 2 *('L' indicates main lobes, 'T' trabeculae, 'K' knees and 'G' grooves).*

particles.

In the plot, continuous lines indicate the phases preceding thrombus formation, transitioning to a dashed lines once the thrombus has formed. For the clarity of representation, in $P_5$ (located beyond the orifice), where the concentrations remain very low and thrombus formation never occurs, dotted black lines are used. In particular, the thrombin concentration in partition 5 consistently hovers around $10^{-10}$ mol/m$^3$ throughout the 80 numerical cycles. This is significantly lower than that observed in the other partitions of the LAA. This finding well aligns with the clinical evidence [97,98], which indicates that thrombin concentration in the LAA is higher than in the atrium.

In partitions 2 and 4, thrombin concentrations continue to rise as the thrombus expands internally within these regions. In contrast, partitions 1 and 3 exhibit distinct patterns in their thrombin concentrations. In partition 1, thrombus formation occurs as early as the 8$^{th}$ cycle, whereas in partition 3, thrombus formation is delayed until the 14$^{th}$ cycle. The thrombin concentration in partition 1 reaches a plateau around the 26$^{th}$ cycle, and subsequently declines at the 62$^{nd}$ cycle; while in partition 3, the concentration begins to decrease at the 77$^{th}$ cycle.

Both partitions 1 and 3 display peaks of activated platelet concentrations at cycles 13 and 27, respectively, followed by sharp declines indicating rapid platelet consumption during thrombus formation.

Although thrombus formation occurs earlier in partition 1, due to reduced blood washout, this partition appears to be at lower risk compared to partition 3. The latter, characterised by a higher washout rate, exhibits a delay in thrombus formation; however, once formed, the clot is more susceptible to detachment and subsequent embolisation (as discussed in sections 3.1 and 3.2). In order to further substantiate this dynamics, the trajectories of several solid particles were monitored over twenty-five numerical cycles. In particular, the trajectory of three

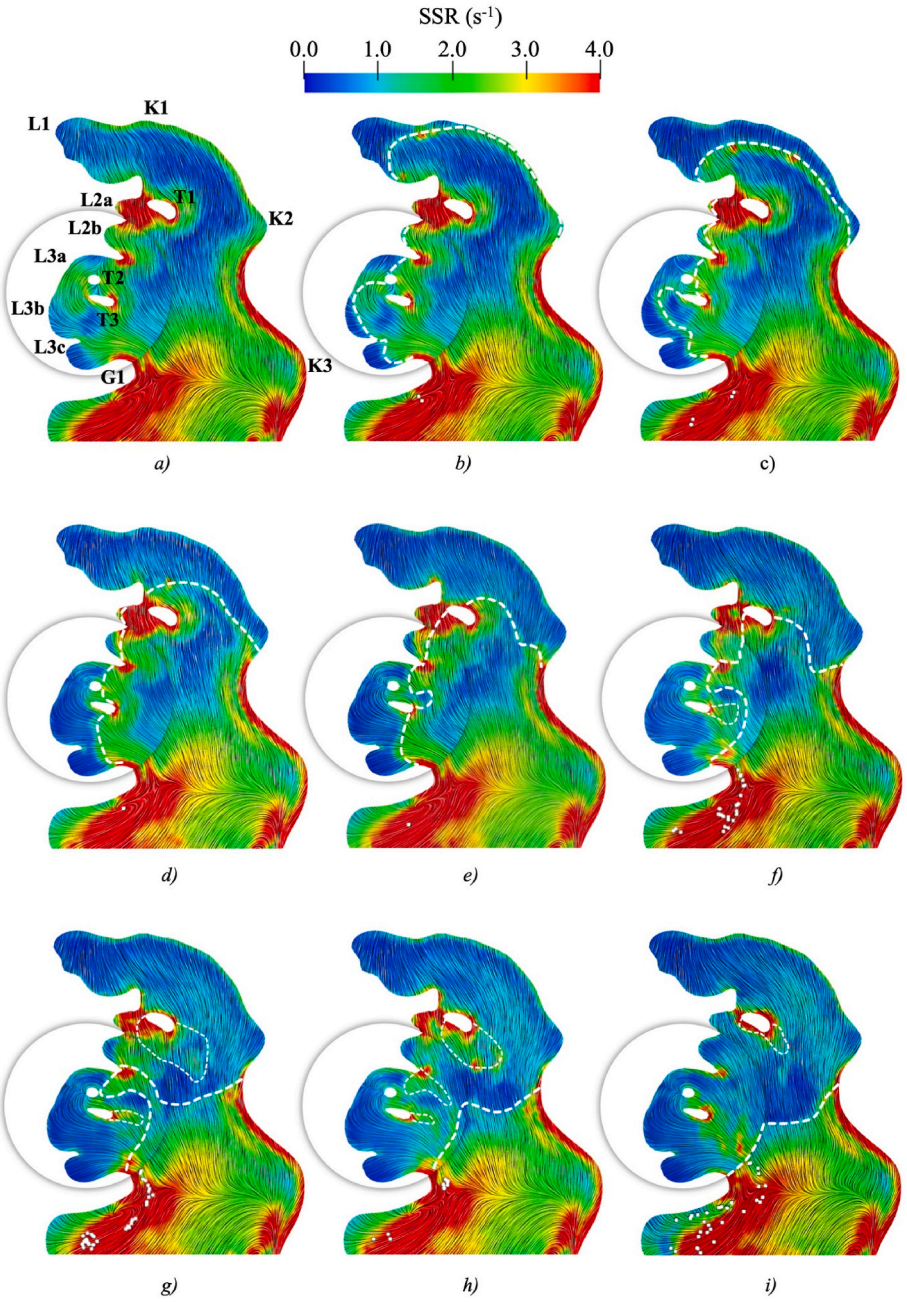


**Fig. 7.** Continuous shear strain rate contour maps and velocity streamline at the time instant $t_2$ corresponding to the minimum volume. Bold white dashed line: thrombus front; thin white dashed line: internal flow channels wall. White dots: emboli. Numerical cycles a to i are indicated in Fig. 4. The local features of the LAA are reported as in Fig. 2 ('L' indicates main lobes, 'T' trabeculae, 'K' knees and 'G' grooves).

particles, coming from the thrombus-blood interface, is shown in Fig. 10: one starting from partition 3 (C) and the other two from partitions 2 and 4 (B and A, respectively), near trabecula T1, after the thrombus developed within the domain. Particle C from partition 3 exits the domain within 16 cycles (from 3$^{rd}$ to 18$^{th}$), due to the high blood washout; while particles A and B from partitions 2 and 4, respectively, remain 'trapped' within the domain.

In summary, the results highlight significant variations in thrombin and activated platelet concentrations across the different partitions of the LAA, which appear to relate to the different levels of thromboembolic risk.

## 4. Limitations

This study has some limitations. Firstly, blood is treated as a Newtonian fluid, which simplifies the complex rheological behaviour of blood. Secondly, the wall movement is modelled as periodic, which is a significant limitation, as the presence of a thrombus might alter the contraction dynamics. To improve the accuracy of the model, future studies will incorporate a more realistic representation of the wall motion, considering its alteration during thrombus growth. Also, the modelling of the coagulation cascade is simplified, and additional biological factors that may influence thrombus formation and stability could be included in the future.

Moreover, this work does not model the left atrium, mitral valve, and pulmonary veins. This simplification, as demonstrated in previous works

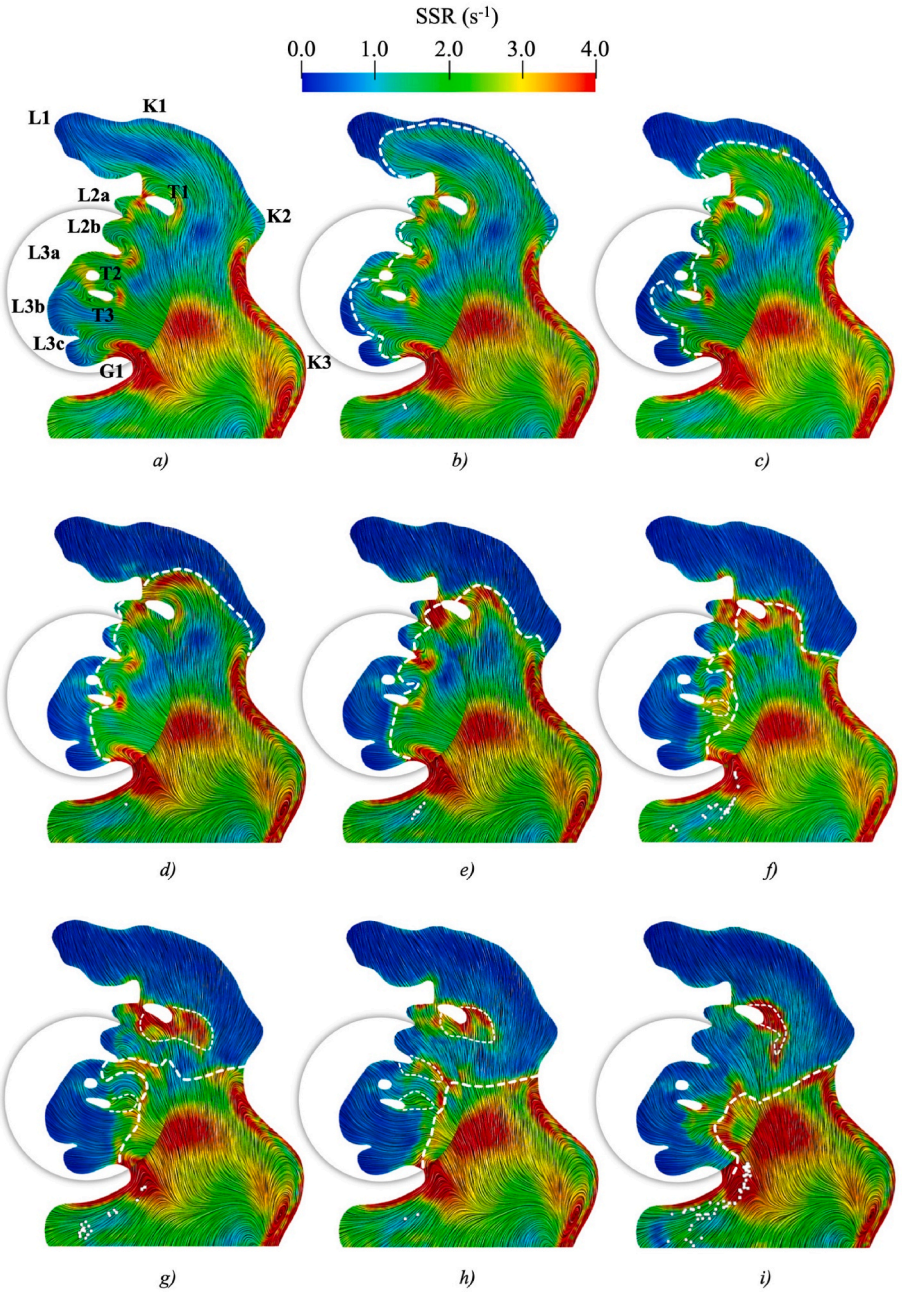


**Fig. 8.** *Continuous shear strain rate contour maps and velocity streamline at the time instant* $t_3$ corresponding to the maximum LAA volume. Bold white dashed line: thrombus front; thin white dashed line: internal flow channels wall. White dots: emboli. Numerical cycles a to i are indicated in Fig. 4. *The local features of the LAA are reported as in* Fig. 2 *('L' indicates main lobes, 'T' trabeculae, 'K' knees and 'G' grooves).*

[24,29], has minimal impact on the fluid dynamics in the LAA regions where flow conditions increase the risk of clot formation [22]. Nevertheless, when more detailed patient-specific simulations are required, the presented computational tool remains suitable for analysing larger regions (e.g. including the left atrium, the pulmonary veins, and the mitral valve).

Finally, a key limitation is the lack of experimental validation and retrospective analyses, which would be crucial for confirming the robustness and accuracy of the approach. Although obtaining such data is challenging, efforts are underway to gather it for future validation.

## 5. Conclusions

This study simulates thrombus formation in a patient-specific left atrial appendage under the pathological condition of AF. To this aim, a mono-physics FSI model based on the meshless SPH method was employed.

The final stages of the coagulation cascade was modelled considering four biochemical species and three types of particles.

In the model, fluid particles switch to solid phase when specific haemodynamic and biochemical conditions occur. Solid particles are treated by incorporating internal spring links between them and are solved in a unique system with fluid particles, consequently obtaining an intrinsic coupling between the fluid and solid phases. The method does not require an interface separating fluid and solid, often necessary in common FSI models, thus simplifying the procedure and reducing computational costs. The particle agglomeration/dissolution algorithm effectively manages thrombus growth, its interaction with blood flow

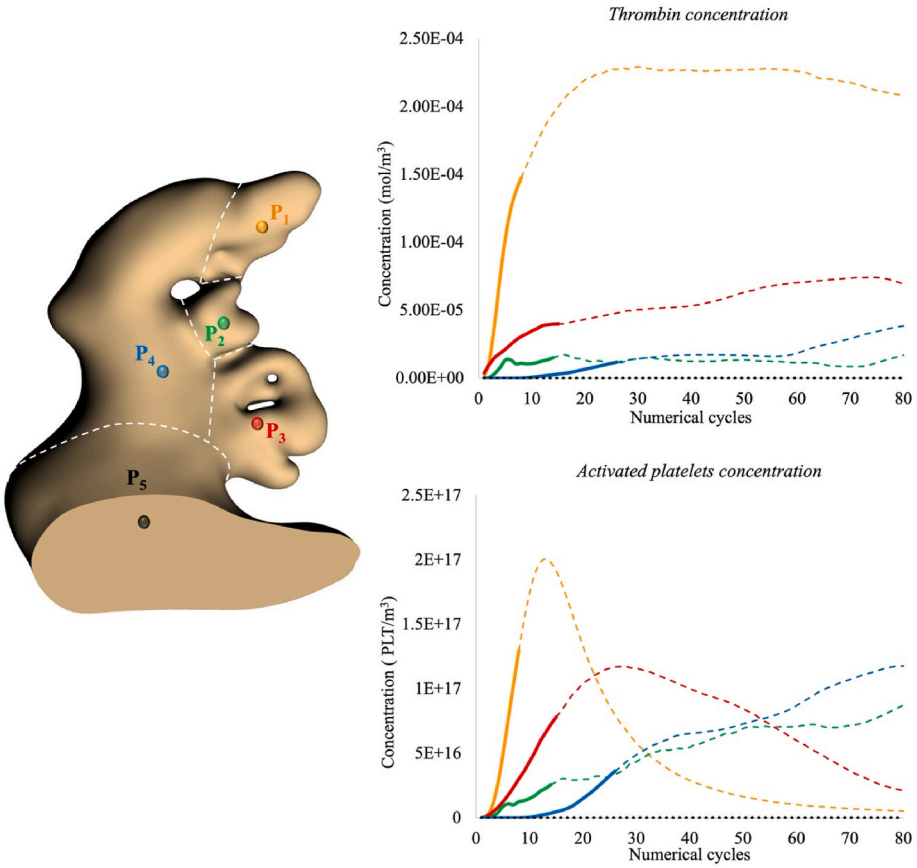


**Fig. 9.** Evolution of thrombin and activated platelets concentrations at the centroid of partitions P1 (orange), P2 (green), P3 (red), P4 (blue) and P5 (black). Continuous and dashed lines: before and after, respectively, the thrombus formation at the centroid; dotted black line: partition P5 where the thrombus never forms. (For interpretation of the references to colour in this figure legend, the reader is referred to the Web version of this article.)


**Fig. 10.** Pathlines of three particles: A starting from partition 4 (monitored during 3rd–27th cycles), B from partition 2 (during 3rd–27th cycles) and C from partition 3 (during 3rd–18$^{th}$cycles).

and, eventually, the formation of emboli.

This is the first study which analyses both the thrombus growth and its evolution as well as the haemodynamic changes that occur during this process.

In accordance with the literature, areas characterised by lower recirculation are notably affected: thrombus formation initiates at the tip of the LAA and gradually expands through the lobes and trabeculae. These areas, which are most prone to thrombus formation, correspond to those predicted by the haemodynamic parameter BSF, previously calculated by Musotto et al. [30] to assess thromboembolic risk in the LAA.

The findings of this study highlight distinct risk profiles across different regions of the LAA. In particular, in the early stages, when thrombus formation is confined to the LAA tip, the analysis suggests that the risk of neurological damage is lower, particularly if diagnosed promptly. However, as the thrombus progresses and reaches areas with higher SSR, the likelihood of embolisation increases, consequently elevating the risk of ischemic events such as stroke.

The LAA tip, where thrombus formation initially occurs, appears to be less prone to embolisation and can be considered safer. In contrast, the region closer to the orifice, while experiencing higher washout effects that delay thrombus accumulation, seems to be more prone to

instability due to increased recirculation. This may contribute to the detachment of emboli and raise the risk of thromboembolic events. These findings underscore the importance of understanding the dynamic progression of clot formation and growth to predict thromboembolic risks more accurately.

By identifying regions most susceptible to embolisation, particularly where thrombi are more likely to detach, clinical decision-making can be improved. Early detection of these high-risk areas allows for timely intervention, potentially preventing or mitigating the severity of embolic events.

A thorough understanding of thrombus formation and its interaction with blood flow is crucial for developing more effective therapeutic strategies, and should ideally be included in the risk criteria. In fact, recognising the critical stages in thrombus evolution, such as the transition from stability to increasing risk of embolisation, can contribute to devise more effective diagnostic approaches and create more precise guidelines, ultimately reducing embolic risks and enhancing patient management in atrial fibrillation.

## CRediT authorship contribution statement

**Anna Maria Lo Presti:** Writing – original draft, Methodology, Formal analysis, Data curation, Conceptualization. **Alessandra Monteleone:** Writing – original draft, Validation, Supervision, Software, Methodology, Investigation, Funding acquisition, Formal analysis, Data curation, Conceptualization. **Giulio Musotto:** Investigation, Data curation, Conceptualization. **Alessandro Tamburini:** Writing – review & editing, Supervision, Funding acquisition. **Enrico Napoli:** Writing – review & editing, Supervision, Software, Methodology, Funding acquisition. **Gaetano Burriesci:** Writing – review & editing, Supervision, Resources, Project administration, Methodology, Investigation, Funding acquisition, Formal analysis, Conceptualization.

## Ethics statement

This study was carried out in accordance with the recommendations of the South East Research Ethics Research Committee, Ayelsford, Kent, United Kingdom, with written informed consent from all subjects. All subjects gave written informed consent in accordance with the Declaration of Helsinki. The protocol was approved by the South East Research Ethics Research Committee, Ayelsford, Kent, United Kingdom. The patients/participants provided their written informed consent to participate in this study.

## Declaration of competing interest

None Declared.

## Acknowledgements

The authors thank Leon Menezes of UCL Institute of Nuclear Medicine, University College London, and Andrew Cook of UCL Institute of Cardiovascular Science and Great Ormond Street Hospital for Children, for acquisition and analysis of medical images. In addition, a special appreciation goes to Giorgia Bosi of UCL Mechanical Engineering, University College London, for the many helpful discussions and support.

This work was supported by *Piano Nazionale di Ripresa e Resilienza* (PNRR) under project 39-033-20-DOT204NJ79-9840, DM 117/2023, Investment 3.3: "*Introduction of innovative doctoral programs addressing the innovation needs of companies and promoting the recruitment of researchers by enterprises*".

## References

[1] G. Lippi, F. Sanchis-Gomar, G. Cervellin, Global epidemiology of atrial fibrillation: an increasing epidemic and public health challenge, Int. J. Stroke 16 (2) (2021) 217–221, https://doi.org/10.1177/1747493019897870.
[2] B.J.J.M. Brundel, X. Ai, M.T. Hills, M.F. Kuipers, G.Y.H. Lip, N.M.S. de Groot, Atrial fibrillation, Nat. Rev. Dis. Primers 8 (1) (2022) 21, https://doi.org/10.1038/s41572-022-00347-9.
[3] F. Rahman, G.F. Kwan, E.J. Benjamin, Global epidemiology of atrial fibrillation, Nat. Rev. Cardiol. 11 (11) (2014) 639–654, https://doi.org/10.1038/nrcardio.2014.118.
[4] B. Freedman, T.S. Potpara, G.Y.H. Lip, Stroke prevention in atrial fibrillation, Lancet 388 (10046) (2016) 806–817, https://doi.org/10.1016/S0140-6736(16)31257-0.
[5] T. Watson, E. Shantsila, G.Y. Lip, Mechanisms of thrombogenesis in atrial fibrillation: Virchow's triad revisited, Lancet 373 (9658) (2009) 155–166, https://doi.org/10.1016/S0140-6736(09)60040-4.
[6] N.M. Al-Saady, O.A. Obel, A.J. Camm, Left atrial appendage: structure, function, and role in thromboembolism, Heart 82 (5) (Nov. 1999) 547–554, https://doi.org/10.1136/hrt.82.5.547.
[7] G. Ernst, et al., Morphology of the left atrial appendage, Anat. Rec. 242 (4) (1995) 553–561, https://doi.org/10.1002/ar.1092420411.
[8] L. Di Biase, et al., Does the left atrial appendage morphology correlate with the risk of stroke in patients with atrial fibrillation? Results from a multicenter study, J. Am. Coll. Cardiol. 60 (6) (2012) 531–538, https://doi.org/10.1016/j.jacc.2012.04.032.
[9] D. Green, Coagulation cascade, Hemodial. Int. 10 (SUPPL. 2) (2006) 10–12, https://doi.org/10.1111/j.1542-4758.2006.00119.x.
[10] A. Qureshi, G.Y.H. Lip, D.A. Nordsletten, S.E. Williams, O. Aslanidi, A. de Vecchi, Imaging and biophysical modelling of thrombogenic mechanisms in atrial fibrillation and stroke, Front. Cardiovasc. Med. 9 (January) (2023) 1–14, https://doi.org/10.3389/fcvm.2022.1074562.
[11] R. Virchow, Thrombosis and Emboli, Canton, Ma, 1856.
[12] B.F. Gage, et al., Selecting patients with atrial fibrillation for anticoagulation: stroke risk stratification in patients taking aspirin, Circulation 110 (16) (2004) 2287–2292, https://doi.org/10.1161/01.CIR.0000145172.55640.93.
[13] J. Steffel, et al., 2021 European heart rhythm association practical guide on the use of non-vitamin K antagonist oral anticoagulants in patients with atrial fibrillation, Europace 23 (10) (2021) 1612–1676, https://doi.org/10.1093/europace/euab065.
[14] G. Ailawadi, et al., Exclusion of the left atrial appendage with a novel device: early results of a multicenter trial, J. Thorac. Cardiovasc. Surg. 142 (5) (2011) 1002–1009.
[15] U. Landmesser, C. Skurk, A. Tzikas, V. Falk, V.Y. Reddy, S. Windecker, Left atrial appendage closure for stroke prevention in atrial fibrillation: current status and perspectives, Eur. Heart J. 45 (32) (2024) 2914–2932, https://doi.org/10.1093/eurheartj/ehae398.
[16] D. Penela, G. Falasconi, G. Zucchelli, Transcatheter options for atrial fibrillation treatment: an overview of the ablative techniques currently available and future perspectives, Ann. Cardiothorac. Surg. 13 (1) (2024) 31–43, https://doi.org/10.21037/acs-2023-afm-0060.
[17] G. Hindricks, et al., 2020 ESC Guidelines for the diagnosis and management of atrial fibrillation developed in collaboration with the European Association for Cardio-Thoracic Surgery (EACTS), Eur. Heart J. 42 (5) (2021) 373–498, https://doi.org/10.1093/eurheartj/ehaa612.
[18] L.T. Zhang, M. Gay, Characterizing left atrial appendage functions in sinus rhythm and atrial fibrillation using computational models, J. Biomech. 41 (11) (2008) 2515–2523, https://doi.org/10.1016/j.jbiomech.2008.05.012.
[19] R. Koizumi, et al., Numerical analysis of hemodynamic changes in the left atrium due to atrial fibrillation, J. Biomech. 48 (3) (2015) 472–478, https://doi.org/10.1016/j.jbiomech.2014.12.025.
[20] T. Otani, A. Al-Issa, A. Pourmorteza, E.R. McVeigh, S. Wada, H. Ashikaga, A computational framework for personalized blood flow analysis in the human left atrium, Ann. Biomed. Eng. 44 (11) (2016) 3284–3294, https://doi.org/10.1007/s10439-016-1590-x.
[21] A.L. Olivares, et al., In silico analysis of haemodynamics in patient-specific left atria with different appendage morphologies, Lect. Notes Comput. Sci. 10263 LNCS (May) (2017) 412–420, https://doi.org/10.1007/978-3-319-59448-4_39.
[22] G.M. Bosi, et al., Computational fluid dynamic analysis of the left atrial appendage to predict thrombosis risk, Front. Cardiovasc. Med. 5 (2018), https://doi.org/10.3389/fcvm.2018.00034.
[23] A. Masci, et al., The impact of left atrium appendage morphology on stroke risk assessment in atrial fibrillation: a computational fluid dynamics study, Front. Physiol. 9 (Jan. 2019), https://doi.org/10.3389/fphys.2018.01938.
[24] D. Vella, A. Monteleone, G. Musotto, G.M.G.M. Bosi, G. Burriesci, Effect of the alterations in contractility and morphology produced by atrial fibrillation on the thrombosis potential of the left atrial appendage, Front. Bioeng. Biotechnol. 9 (Feb. 2021) 147, https://doi.org/10.3389/fbioe.2021.586041.
[25] H.A. Kjeldsberg, et al., Impact of left atrial wall motion assumptions in fluid simulations on proposed predictors of thrombus formation, Int. j. numer. method. biomed. eng. 40 (6) (2024) 1–20, https://doi.org/10.1002/cnm.3825.
[26] A. Zingaro, et al., A comprehensive stroke risk assessment by combining atrial computational fluid dynamics simulations and functional patient data, Sci. Rep. 14 (1) (2024) 1–17, https://doi.org/10.1038/s41598-024-59997-2.
[27] A. Masci, et al., A Proof of concept for computational fluid dynamic analysis of the left atrium in atrial fibrillation on a patient-specific basis, J. Biomech. Eng. 142 (1) (2020) 1–11, https://doi.org/10.1115/1.4044583.

[28] M. García-Villalba, et al., Demonstration of patient-specific simulations to assess left atrial appendage thrombogenesis risk, Front. Physiol. 12 (February) (2021) 1–14, https://doi.org/10.3389/fphys.2021.596596.
[29] G. Musotto, et al., The role of patient-specific morphological features of the left atrial appendage on the thromboembolic risk under atrial fibrillation, Front. Cardiovasc. Med. 9 (Jul. 2022), https://doi.org/10.3389/fcvm.2022.894187.
[30] G. Musotto, et al., Fluid-structure interaction analysis of the thromboembolic risk in the left atrial appendage under atrial fibrillation: effect of hemodynamics and morphological features, Comput. Methods Programs Biomed. 246 (February) (2024) 108056, https://doi.org/10.1016/j.cmpb.2024.108056.
[31] J. Yang, et al., Research on the internal flow field of left atrial appendage and stroke risk assessment with different blood models, Bioengineering 10 (8) (2023), https://doi.org/10.3390/bioengineering10080944.
[32] X. Morales Ferez, et al., Deep learning framework for real-time estimation of in-silico thrombotic risk indices in the left atrial appendage, Front. Physiol. 12 (June) (2021) 1–14, https://doi.org/10.3389/fphys.2021.694945.
[33] Y. Wang, B. Xu, K. Luo, J. Fan, M. Xiang, The impact of left atrial morphology on thrombosis risk in atrial fibrillation, Phys. Fluids 36 (7) (2024), https://doi.org/10.1063/5.0214185.
[34] A. Qureshi, et al., MRI-based modelling of left atrial flow and coagulation to predict risk of thrombogenesis in atrial fibrillation, Med. Image Anal. 101 (January) (2025) 103475, https://doi.org/10.1016/j.media.2025.103475.
[35] B. Xu, et al., Identifying left atrium and left atrial appendage prone to thrombus formation in patients with atrial fibrillation using statistical shape modeling, Int. J. Cardiol. 420 (June 2024) (2025) 132731, https://doi.org/10.1016/j.ijcard.2024.132731.
[36] L. Parker, et al., A multi-modal computational fluid dynamics model of left atrial fibrillation haemodynamics validated with 4D flow MRI, Biomech. Model. Mechanobiol. (2025) 0123456789, https://doi.org/10.1007/s10237-024-01901-y.
[37] M. Falanga, C. Cortesi, A. Chiaravalloti, A.D. Monte, C. Tomasi, C. Corsi, A digital twin approach for stroke risk assessment in Atrial Fibrillation Patients, Heliyon 10 (20) (2024) e39527, https://doi.org/10.1016/j.heliyon.2024.e39527.
[38] J. Yang, C. Song, H. Ding, M. Chen, J. Sun, X. Liu, Numerical study of the risk of thrombosis in the left atrial appendage of chicken wing shape in atrial fibrillation, Front. Cardiovasc. Med. 9 (November) (2022) 1–12, https://doi.org/10.3389/fcvm.2022.985674.
[39] Y. Chen, B. Xu, Y. Cheng, K. Luo, J. Fan, M. Xiang, Hemodynamic differences caused by left atrial appendage modeling contours, Phys. Fluids 35 (11) (2023), https://doi.org/10.1063/5.0172261.
[40] N. Paliwal, et al., Slow blood-flow in the left atrial appendage is associated with stroke in atrial fibrillation patients, Heliyon 10 (5) (2024) e26858, https://doi.org/10.1016/j.heliyon.2024.e26858.
[41] M. Koupenova, B.E. Kehrel, H.A. Corkrey, J.E. Freedman, Thrombosis and platelets: an update, Eur. Heart J. (Dec. 2016) ehw550, https://doi.org/10.1093/eurheartj/ehw550.
[42] Z. Zhang, J. Zhu, M. Wu, M. Neidlin, W.T. Wu, P. Wu, Computational modeling of hemodynamics and risk of thrombosis in the left atrial appendage using patient-specific blood viscosity and boundary conditions at the mitral valve, Biomech. Model. Mechanobiol. 22 (4) (2023) 1447–1457, https://doi.org/10.1007/s10237-023-01731-4.
[43] A. Gonzalo, et al., Non-Newtonian blood rheology impacts left atrial stasis in patient-specific simulations, Int. j. numer. method. biomed. eng. 38 (6) (2022) 1–23, https://doi.org/10.1002/cnm.3597.
[44] Q. Gao, et al., A deep learning model for efficient end-to-end stratification of thrombotic risk in left atrial appendage, Eng. Appl. Artif. Intell. 126 (April) (2023), https://doi.org/10.1016/j.engappai.2023.107187.
[45] X. Liu, et al., LAFlowNet: a dynamic graph method for the prediction of velocity and pressure fields in left atrium and left atrial appendage, Eng. Appl. Artif. Intell. 136 (PA) (2024) 108896, https://doi.org/10.1016/j.engappai.2024.108896.
[46] R.A. Gingold, J.J. Monaghan, Smoothed particle hydrodynamics: theory and application to non-spherical stars, Mon. Not. R. Astron. Soc. 181 (181) (Dec. 1977) 375–389, https://doi.org/10.1093/mnras/181.3.375.
[47] M. Kojic, N. Filipovic, B. Stojanovic, N. Kojic, Discrete particle methods for modeling of solids and fluids, in: Computer Modeling in Bioengineering, 2008, pp. 147–170, https://doi.org/10.1002/9780470751763.ch8.
[48] F. Wang, et al., Particle hydrodynamic simulation of thrombus formation using velocity decay factor, Comput. Methods Programs Biomed. 207 (Aug. 2021) 106173, https://doi.org/10.1016/j.cmpb.2021.106173.
[49] M. Al-Saad, C.A. Suarez, A. Obeidat, S.P.A. Bordas, S. Kulasegaram, Application of smooth particle hydrodynamics method for modelling blood flow with Thrombus Formation, Comput. Model. Eng. Sci. 122 (3) (2020) 831–862, https://doi.org/10.32604/cmes.2020.08527.
[50] T. Ye, H. Shi, N. Phan-Thien, C.T. Lim, The key events of thrombus formation: platelet adhesion and aggregation, Biomech. Model. Mechanobiol. 19 (3) (Jun. 2020) 943–955, https://doi.org/10.1007/s10237-019-01262-x.
[51] A. Monteleone, A. Viola, E. Napoli, G. Burriesci, Modelling of thrombus formation using smoothed particle hydrodynamics method, PLoS One 18 (2) (Feb. 2023) e0281424, https://doi.org/10.1371/journal.pone.0281424.
[52] J.O. Taylor, et al., In vitro quantification of time dependent thrombus size using magnetic resonance imaging and computational simulations of thrombus surface shear stresses, J. Biomech. Eng. 136 (7) (Jul. 2014), https://doi.org/10.1115/1.4027613.
[53] K.N. Shankar, Y. Zhang, T. Sinno, S.L. Diamond, A three-dimensional multiscale model for the prediction of thrombus growth under flow with single-platelet resolution, PLoS Comput. Biol. 18 (1) (2022) 1–19, https://doi.org/10.1371/journal.pcbi.1009850.
[54] L. Yang, N. Tobin, K.B. Manning, Refining a numerical model for device-induced thrombosis and investigating the effects of non-Newtonian blood models, J. Biomech. 120 (2021) 110393, https://doi.org/10.1016/j.jbiomech.2021.110393.
[55] W.T. Wu, M.A. Jamiolkowski, W.R. Wagner, N. Aubry, M. Massoudi, J.F. Antaki, Multi-constituent simulation of thrombus deposition, Sci. Rep. 7 (September 2016) (2017) 1–16, https://doi.org/10.1038/srep42720.
[56] C. Menichini, X.Y. Xu, Mathematical modeling of thrombus formation in idealized models of aortic dissection: initial findings and potential applications, J. Math. Biol. 73 (5) (Nov. 2016) 1205–1226, https://doi.org/10.1007/s00285-016-0986-4.
[57] A. Bouchnita, V. Volpert, N. Kozulinas, A.V. Belyaev, G. Panasenko, Multiphase patient-specific simulations to study fibrillation-induced thrombosis in the left atrial appendage, Phys. Fluids 36 (7) (2024), https://doi.org/10.1063/5.0216196.
[58] H. Wendland, Piecewise polynomial, positive definite and compactly supported radial functions of minimal degree, Adv. Comput. Math. 4 (1) (Dec. 1995) 389–396, https://doi.org/10.1007/BF02123482.
[59] E. Napoli, M. De Marchis, E. Vitanza, PANORMUS-SPH. A new Smoothed Particle Hydrodynamics solver for incompressible flows, Comput. Fluids 106 (2015) 185–195, https://doi.org/10.1016/j.compfluid.2014.09.045.
[60] E. Napoli, M. De Marchis, C. Gianguzzi, B. Milici, A. Monteleone, A coupled finite volume–smoothed particle hydrodynamics method for incompressible flows, Comput. Methods Appl. Mech. Eng. 310 (Oct. 2016) 674–693, https://doi.org/10.1016/j.cma.2016.07.034.
[61] A. Monteleone, M. De Marchis, B. Milici, E. Napoli, A multi-domain approach for smoothed particle hydrodynamics simulations of highly complex flows, Comput. Methods Appl. Mech. Eng. 340 (Oct. 2018) 956–977, https://doi.org/10.1016/j.cma.2018.06.029.
[62] A. Monteleone, M. Monteforte, E. Napoli, Inflow/outflow pressure boundary conditions for smoothed particle hydrodynamics simulations of incompressible flows, Comput. Fluids 159 (2017), https://doi.org/10.1016/j.compfluid.2017.09.011.
[63] H.A. van der Vorst, H.A. van der Vorst, H.A. van der Vorst, Bi-CGSTAB: a fast and smoothly converging variant of Bi-CG for the solution of nonsymmetric linear systems, SIAM J. Sci. Stat. Comput. 13 (2) (Mar. 1992) 631–644, https://doi.org/10.1137/0913035.
[64] A.J. Chorin, Numerical solution of the Navier-Stokes equations, Math. Comput. 22 (104) (1968) 745–762, https://doi.org/10.1090/S0025-5718-1968-0242392-2.
[65] J.W. Swegle, D.L. Hicks, S.W. Attaway, Smoothed particle hydrodynamics stability analysis, J. Comput. Phys. 116 (1) (Jan. 1995) 123–134, https://doi.org/10.1006/jcph.1995.1010.
[66] R. Xu, P. Stansby, D. Laurence, Accuracy and stability in incompressible SPH (ISPH) based on the projection method and a new approach, J. Comput. Phys. 228 (18) (Oct. 2009) 6703–6725, https://doi.org/10.1016/j.jcp.2009.05.032.
[67] M. Guerrero-Hurtado, et al., Efficient multi-fidelity computation of blood coagulation under flow, PLoS Comput. Biol. 19 (10 October) (2023) 1–25, https://doi.org/10.1371/journal.pcbi.1011583.
[68] W. Bergmeier, et al., The role of platelet adhesion receptor GPIbα far exceeds that of its main ligand, von Willebrand factor, in arterial thrombosis, Proc. Natl. Acad. Sci. U. S. A. 103 (45) (2006) 16900–16905, https://doi.org/10.1073/pnas.0608207103.
[69] Maureane Hoffman, Remodeling the blood coagulation cascade, J. Thromb. Thrombolysis 16 (1–2) (2003) 17–20.
[70] E.N. Sorensen, G.W. Burgreen, W.R. Wagner, J.F. Antaki, Computational simulation of platelet deposition and activation: I. Model development and properties, Ann. Biomed. Eng. 27 (4) (1999) 436–448, https://doi.org/10.1114/1.200.
[71] M. Anand, K. Rajagopal, K.R. Rajagopal, A model incorporating some of the mechanical and biochemical factors underlying clot formation and dissolution in flowing blood, J. Theor. Med. 5 (3–4) (2003) 183–218, https://doi.org/10.1080/10273660412331317415.
[72] A. Sarrami-Foroushani, T. Lassila, S.M. Hejazi, S. Nagaraja, A. Bacon, A.F. Frangi, A computational model for prediction of clot platelet content in flow-diverted intracranial aneurysms, J. Biomech. 91 (Jun. 2019) 7–13, https://doi.org/10.1016/j.jbiomech.2019.04.045.
[73] K. Leiderman, A.L. Fogelson, Grow with the flow: a spatial-temporal model of platelet deposition and blood coagulation under flow, Math. Med. Biol. 28 (1) (Mar. 2011) 47–84, https://doi.org/10.1093/imammb/dqq005.
[74] B. Ingalls, Mathematical Modeling in Systems Biology: an Introduction, MIT Press, 2013.
[75] T. Jiao, M. Ye, M. Jin, J. Yang, An interactively corrected smoothed particle hydrodynamics (IC-SPH) for simulating solute transport in a nonuniform velocity field, Water Resour. Res. 58 (6) (2022) 1–25, https://doi.org/10.1029/2021WR031017.
[76] P.A. Herrera, M. Massabó, R.D. Beckie, A meshless method to simulate solute transport in heterogeneous porous media, Adv. Water Resour. 32 (3) (2009) 413–429, https://doi.org/10.1016/j.advwatres.2008.12.005.
[77] Y.S. Chang, T.J. Chang, SPH simulations of solute transport in flows with steep velocity and concentration gradients, Water (Switzerland) 9 (2) (2017), https://doi.org/10.3390/w9020132.
[78] Y. Zhu, P.J. Fox, Smoothed particle hydrodynamics model for diffusion through porous media, Transp. Porous Media 43 (3) (2001) 441–471, https://doi.org/10.1023/A:1010769915901.
[79] Z. Wang, O. Delestre, D.Q. Hou, J. Wei, J. Dang, SPH simulation of pollutant transport in rivers, Iccte (2016) 629–632, https://doi.org/10.2991/iccte-16.2016.105.

[80] Z. Sun, Q. Hou, A.S. Tijsseling, J. Lian, J. Wei, Smoothed particle hydrodynamics with diffusive flux for advection–diffusion equation with discontinuities, Comput. Math. Appl. 160 (December 2023) (2024) 70–85, https://doi.org/10.1016/j.camwa.2024.02.012.
[81] W. Liu, Q. Hou, J. Lian, A. Zhang, J. Dang, Coastal pollutant transport modeling using smoothed particle hydrodynamics with diffusive flux, Adv. Water Resour. 146 (June) (2020) 103764, https://doi.org/10.1016/j.advwatres.2020.103764.
[82] T. Jiao, M. Ye, M. Jin, J. Yang, A finite particle method (FPM) for Lagrangian simulation of conservative solute transport in heterogeneous porous media, Adv. Water Resour. 156 (May) (2021) 104043, https://doi.org/10.1016/j.advwatres.2021.104043.
[83] R.B. Bird, W.E. Stewart, E.N. Lightfoot, Transport phenomena 52 (3) (2002).
[84] H.J. Weiss, Platelets: Pathophysiology and Antiplatelet Drug Therapy, Liss, 1982.
[85] N. Mackman, New insights into the mechanisms of venous thrombosis, J. Clin. Investig. 122 (7) (Jul. 2012) 2331–2336, https://doi.org/10.1172/JCI60229.
[86] N. Grande Gutiérrez, D. Mukherjee, D. Bark, Decoding thrombosis through code: a review of computational models, J. Thromb. Haemost. 22 (1) (2024) 35–47, https://doi.org/10.1016/j.jtha.2023.08.021.
[87] A. Monteleone, S. Di Leonardo, E. Napoli, G. Burriesci, A novel mono-physics particle-based approach for the simulation of cardiovascular fluid-structure interaction problems, Comput. Methods Programs Biomed. 245 (Mar. 2024) 108034, https://doi.org/10.1016/j.cmpb.2024.108034.
[88] A. Monteleone, G. Borino, E. Napoli, G. Burriesci, Fluid–structure interaction approach with smoothed particle hydrodynamics and particle–spring systems, Comput. Methods Appl. Mech. Eng. 392 (Mar. 2022) 114728, https://doi.org/10.1016/j.cma.2022.114728.
[89] S.K. Chimakurthi, S. Reuss, M. Tooley, S. Scampoli, ANSYS Workbench System Coupling: a state-of-the-art computational framework for analyzing multiphysics problems, Eng. Comput. 34 (2) (Apr. 2018) 385–411, https://doi.org/10.1007/s00366-017-0548-4.
[90] J. Park, et al., High left atrial pressures are associated with advanced electroanatomical remodeling of left atrium and independent predictors for clinical recurrence of atrial fibrillation after catheter ablation, Hear. Rhythm 11 (6) (Jun. 2014) 953–960, https://doi.org/10.1016/j.hrthm.2014.03.009.
[91] A. Ducci, F. Pirisi, S. Tzamtzis, G. Burriesci, Transcatheter aortic valves produce unphysiological flows which may contribute to thromboembolic events: an in-vitro study, J. Biomech. 49 (16) (2016) 4080–4089, https://doi.org/10.1016/j.jbiomech.2016.10.050.
[92] A. Monteleone, G. Burriesci, E. Napoli, A distributed-memory MPI parallelization scheme for multi-domain incompressible SPH, J. Parallel Distrib. Comput. 170 (Dec. 2022) 53–67, https://doi.org/10.1016/j.jpdc.2022.08.004.
[93] A. Ruiz-Arango, C. Landolfo, A novel approach to the diagnosis of left atrial appendage thrombus using contrast echocardiography and power Doppler imaging, Eur. J. Echocardiogr. 9 (2) (2008) 329–333, https://doi.org/10.1093/ejechocard/jen068.
[94] B. Kreidieh, M. Valderrábano, Malignant left atrial appendage morphology and embolization risk in atrial fibrillation, Hear. Case Reports 1 (6) (2015) 406–410, https://doi.org/10.1016/j.hrcr.2015.02.016.
[95] M. Yamamoto, et al., Complex left atrial appendage morphology and left atrial appendage thrombus formation in patients with atrial fibrillation, Circ. Cardiovasc. Imaging 7 (2) (2014) 337–343, https://doi.org/10.1161/CIRCIMAGING.113.001317.
[96] S. Bäck, et al., Elevated atrial blood stasis in paroxysmal atrial fibrillation during sinus rhythm: a patient-specific computational fluid dynamics study, Front. Cardiovasc. Med. 10 (August) (2023) 1–10, https://doi.org/10.3389/fcvm.2023.1219021.
[97] K. Bartus, et al., Coagulation factors and fibrinolytic activity in the left atrial appendage and other heart chambers in patients with atrial fibrillation: is there a local intracardiac prothrombotic state? (HEART-CLOT study), Int. J. Cardiol. 301 (2020) 103–107, https://doi.org/10.1016/j.ijcard.2019.09.053.
[98] A. Elias, et al., Elevated thrombin generation levels in the left atrial appendage in patients with atrial fibrillation, Res. Pract. Thromb. Haemost. 7 (2) (2023) 100127, https://doi.org/10.1016/j.rpth.2023.100127.